University of Nevada, Reno

Atmospheric Water Harvesting Using Thermoelectric Peltier Coolers: Single Module and Prototype Characterizations and Design

A thesis submitted in partial fulfillment of the
requirements for the degree of Master of Science in
Electrical Engineering

by

Jose A. Cano Perez

Dr. Xiaoshan Zhu/Thesis Advisor

May 2024

THE GRADUATE SCHOOL

We recommend that the thesis
prepared under our supervision by

JOSE A. CANO PEREZ

entitled

Atmospheric Water Harvesting Using Thermoelectric Peltier Coolers: Single Module and Prototype Characterizations and Design

be accepted in partial fulfillment of the
requirements for the degree of

Master of Science

Xiaoshan Zhu, Ph.D.
Advisor

Jeongwon Park, Ph.D.
Committee Member

Mustafa Hadj-Nacer, Ph.D.
Graduate School Representative

Markus Kemmelmeier, Ph.D., Dean
Graduate School

May, 2024

ABSTRACT

Atmospheric water harvesting is a promising technology that offers a sustainable solution to the water scarcity problem many regions worldwide face. Collecting water vapor from the air provides an alternative source of clean drinking water, especially in arid and semi-arid areas where conventional water sources are limited. One of the critical challenges in atmospheric water harvesting is the need for efficient cooling systems to condense the water vapor from the air. In this regard, thermoelectric coolers have emerged as a promising technology to enhance the performance of atmospheric water harvesters because they are reliable and low maintenance. Unlike traditional cooling systems that rely on mechanical components such as compressors and refrigerants, thermoelectric coolers have no moving parts, making them less prone to wear and tear. This results in a more robust and long-lasting cooling system for atmospheric water harvesters, which is crucial for an effective and sustainable operation, particularly in remote and off-grid locations. Therefore, a fully developed atmospheric water harvesting prototype is designed to utilize thermoelectric coolers to harvest atmospheric water, and it can quickly adapt to solar photovoltaics as a power source. The prototype is the size of a desktop coffee machine. It can be scaled up to address different applications that will address the water challenge for today and tomorrow in Nevada.

ACKNOWLEDGMENTS

First, I would like to express my utmost sincere gratitude to the UNR Electrical Engineering Department, the Bean Space Foundation, and the UNR Mechanical Engineering Department for the courteous counsel and professional help I was given throughout this challenging endeavor. The first person I would like to express my gratitude to is my advisor, Dr. Xiaoshan Zhu, for sharing his expertise. The challenges encountered throughout this project were overcome with his responsible guidance, persistent encouragement, and patience.

Along with Dr. Zhu, I want to thank all my committee members, Dr. Jengwon Park and Dr. Mustafa Hadj-Nacer, for the time and energy they contributed to my education. I would also like to thank Dr. Sami Fadali for setting up a station in the Analog Controls Lab to perform all my experiments and our department staff. Finally, I am grateful to my family for their unconditional support.

TABLE OF CONTENT

LIST OF TABLES

LIST OF FIGURES

CHAPTER 1: INTRODUCTION, OBJECTIVES AND BACKGROUND

1.1 Introduction

As the global population grows and natural freshwater sources are strained, the need for potable water collection intensifies. This escalating demand prompts the consideration and potential adoption of once economically impractical methods. Locally, the state of Nevada has unique geographic and climatic conditions, with its arid desert landscape and limited water resources, making water management a critical issue for the state's economy and development. With limited rainfall and a predominance of arid lands, efficient water use and management strategies are crucial for the sector's sustainability. One potential solution to this problem is atmospheric water harvesters, a reliable and adaptable solution for water collection, particularly in regions facing water scarcity.

1.2 Objective

This endeavor aims to assess and optimize the feasibility of actively extracting water from the atmosphere in a controlled and uncontrolled lab environment. Testing in a controlled environment will ensure scientific development's validity, reliability, safety, and ethical integrity. However, testing in an uncontrolled manner will ensure that actual world conditions can be met, exposing and addressing risks and vulnerabilities that the AWH could encounter when deployed for competitive value. The objective of this development is the optimization of active water harvesting through thermoelectric dehumidification techniques by theoretically mirroring thermophysical factoids, such as temperature, humidity, pressure, heat transfer, surface area, and water vapor properties in the tuning of the system. Such a theoretical framework will serve as a core guideline in selecting the adequate material for the construction of the AWH.

1.3 Background

1.3.1 Local Weather and Fog Information

Nevada has an average annual precipitation rate of 9.5 inches. The southern region of Nevada accounts for nearly three-quarters of the state's water demand and averages only four inches of precipitation per year. The region's water demands are projected to increase by 85 percent by 2065. Nevada's desert climate, growing population, and ongoing drought stress the state's existing water supply, making water efficiency critical. [2]. Nevada has great climatic diversity, such as bright sunshine, slight annual precipitation (averaging nine inches in the valleys and deserts), heavy snowfall in the higher mountains, clean, dry air, and extensive daily temperature ranges [3]. Atmospheric water harvesting emerges as a promising solution to mitigate water scarcity in regions like the Southwest and Nevada, where freshwater resources are limited. This approach can provide sustainable water for various sectors, including agriculture and decentralized water production while addressing logistical challenges in rural areas by diminishing reliance on long-distance water transport [4]. By leveraging Nevada's abundant renewable energy sources, atmospheric water harvesting has the potential to bolster water supplies significantly, fostering economic competitiveness and facilitating population growth in water-stressed regions.

1.3.2 Worldwide Applicable Regions

Various methods for obtaining usable water have been investigated in regions facing severe water scarcity. While basic water collection techniques may seem straightforward, they are essential considerations before the task becomes too challenging, costly, or inefficient. When rainfall is insufficient to sustain freshwater sources, tapping into groundwater through well digging becomes a viable option to secure this precious resource [4]. Other regions, particularly in the southern coastal area of the Arabian Gulf, in the Basra governorate of Iraq, endure persistent high humidity levels year-round, with an average annual humidity of 60.6%. However, the increasing salinity of the Shatt-Al-Arab River, the primary source of drinking water for Basra, due to the intrusion of Gulf waters, has led to a shortage of potable water. Compounding this issue are frequent power outages, which are exacerbated by Basra's status as one of the hottest cities globally [5].

Therefore, there is a pressing need to develop an effective method to extract water from the air in this region, where humidity is high, and an alternative drinking water source is critical. Yet the growing scarcity of freshwater worldwide, exacerbated by climate change and population growth, presents an ongoing challenge that demands attention [6]. Exploring new avenues to prepare for the inevitable water shortages adequately is imperative.

1.4 Types of Atmospheric Water Harvesting Techniques

Water scarcity is a pressing global concern. Air-water generators have been developed to address this, utilizing various techniques such as vapor compression, air compression, Peltier cooling, and desiccation (Figures 1.1 and 1.2). However, fog collectors, while effective in regions with high relative humidity, are limited in their commercial availability due to challenges in meeting crucial commercialization criteria, including efficiency, cost-effectiveness, scalability, broad applicability, and stability [7].

Dew harvesters are a versatile solution, collecting water from dew formation on surfaces at night when temperatures drop below the dew point. They are particularly suitable for arid and semi-arid regions where dew formation is significant during specific periods. Their unique characteristics include a surface with high thermal conductivity to facilitate dew formation. They are relatively simple, have a low-cost design, and their efficiency is influenced by surface material, geometry, and local climate conditions [8].

Fog collectors are effective in coastal areas or regions with frequent fog occurrences. They capture water droplets from fog passing through a mesh or net-like structure, allowing them to merge and drip into collection channels. Mesh materials are optimized to maximize droplet capture while minimizing wind resistance. They can be deployed in large arrays to increase water collection efficiency. However, it's important to note that they require periodic maintenance to prevent clogging and ensure optimal performance, a factor that should be considered in their feasibility [9].

Passive condensation-based harvesters use temperature differentials to condense water vapor from the air onto a cold surface, such as a metal or polymer sheet. It relies on natural

temperature variations, such as day-night cycles, to drive condensation. They are suitable for regions with moderate to high humidity levels and can be integrated into building designs or other structures for decentralized water production. However, efficiency depends on the surface material, insulation, and thermal properties [10].

Active condensation-based harvesters use mechanical or electrical means to create and maintain temperature differentials for water vapor condensation. They utilize energy input to enhance water collection rates, making them suitable for a broader range of climates. They often incorporate refrigeration or thermoelectric cooling systems to create cold surfaces and can be scaled up for larger water production capacities. However, they require energy input, which may limit their applicability in off-grid or remote locations [10].

Hybrid harvesters combine water collection mechanisms, such as condensation, fog collection, and dew harvesting, to maximize water yield across varying environmental conditions. By utilizing complementary water collection methods, they offer versatility and resilience. They can adapt to changing weather patterns and climate conditions for consistent water production. However, they require careful design and integration of multiple components for optimal performance [5].

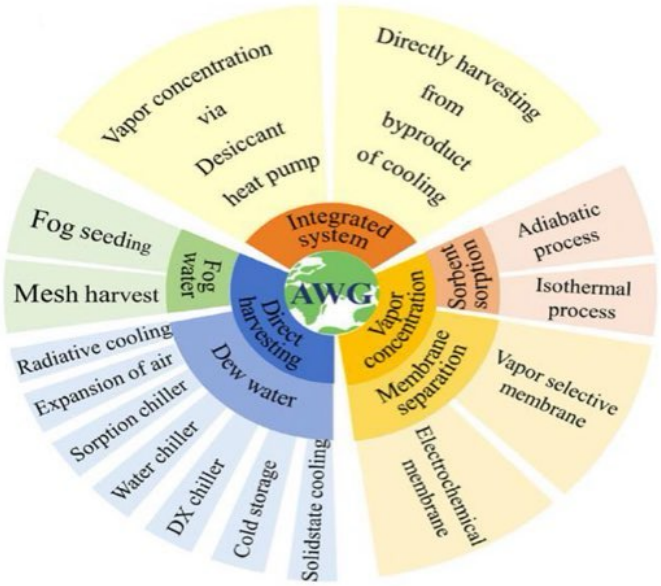

Figure 1.1: Technical categorization of Atmospheric Water Harvesting (AWH) [7].

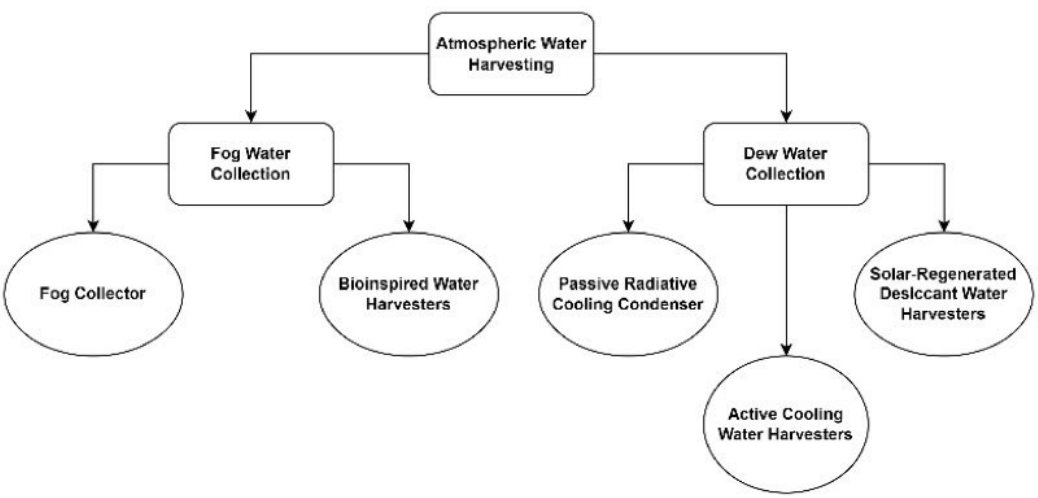

Figure 1.2: Atmospheric Water Harvesting Techniques and Categories [11].

1.4.1 Absorption-based Atmospheric Water Harvesters

Moisture harvesting, enabled by materials with a strong water affinity, operates differently from traditional methods reliant on surface cooling. These materials facilitate spontaneous vapor sorption by effectively trapping water molecules from the air and concentrating moisture. They function efficiently even in low or saturated RH conditions, utilizing adsorption and absorption mechanisms [12].

Figure 1.3 shows an absorption-based AWH. The device consists of two adsorbent layers separated by air gaps, with each layer composed of adsorbent material packed inside a porous metal foam for enhanced thermal conductivity. During the day, the device is heated from the top by sunlight, and during the night, it is opened to expose the adsorbent layers to ambient air for water vapor absorption [13].

Outdoor experiments with the dual-stage prototype yielded approximately 60 mL of water (0.77 L/m2/day) [13]. However, findings suggest that a solar absorber temperature of around 90°C is critical for enhancing performance. Another downside is the high heat capacity and heat loss from the solar absorber, which limits the dual-stage configuration's potential for higher water productivity [12], [13], [14].

Another example is shown in Figure 4. The prototype comprises a sorbent (specifically, silica gel in this case) exposed to radiant energy, a water sorbent unit, a condenser, and a reflector. Experimental trials conducted indoors under controlled conditions such as ambient temperature (22°C), relative humidity (30% to 60%), silica gel thickness (25mm to 35mm), surface area to volume ratio (0.29 to 0.4), and radiant heat flux (509 to 556 W/m2), show that the prototype can yield up to 159g of water per 1kg of silica gel in a 12-

hour cycle under 556 W/m2 radiant flux. Daily, this translated to 800mL of water with an overall efficiency of 50% for a 25mm silica layer thickness [15]. The research team concluded that higher relative humidity could accelerate the adsorption cycle and enhance water capture, release, and collection rates. Enhancements to the system include incorporating multiple layers of sorbent and utilizing materials with superior adsorption and desorption properties [7], [15]

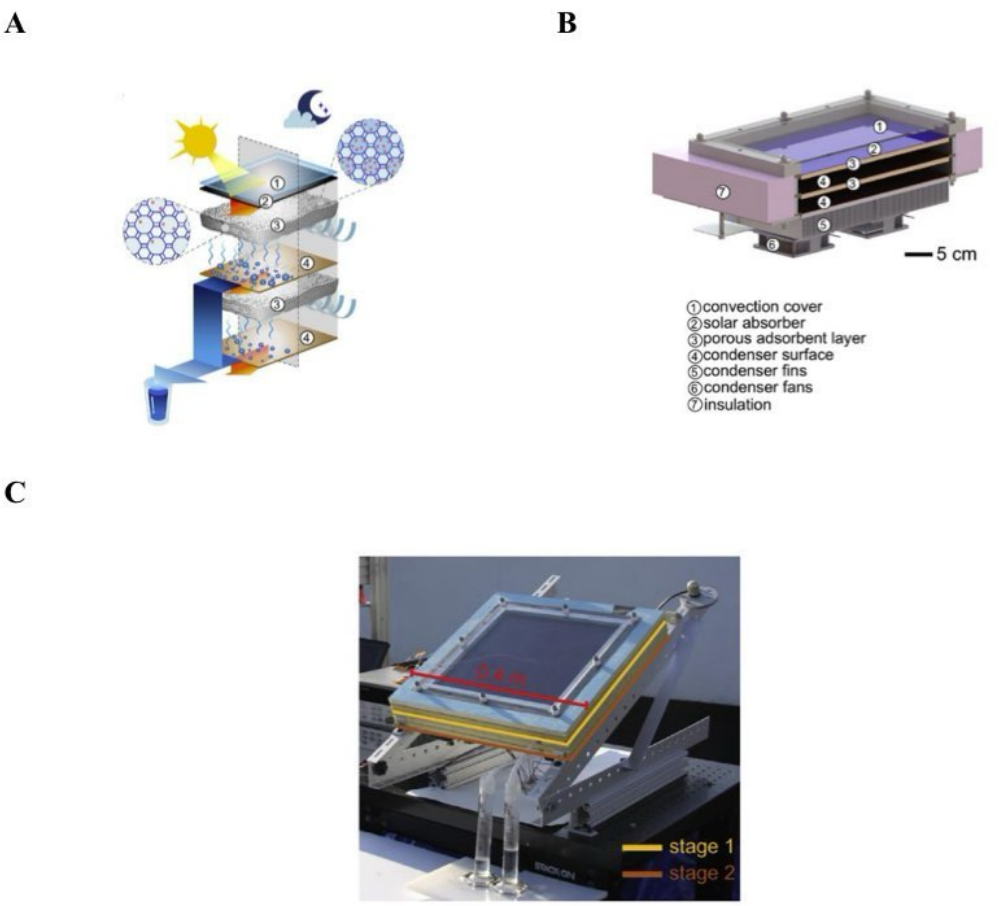

Figure 1.3: A) Dual stage AWH concept. B) 3D- model of the Dual stage AWH concept. C) Dual-stage prototype. Condensed water is drained from tubes at the bottom of each stage into separate graduated cylinders for collection [13].

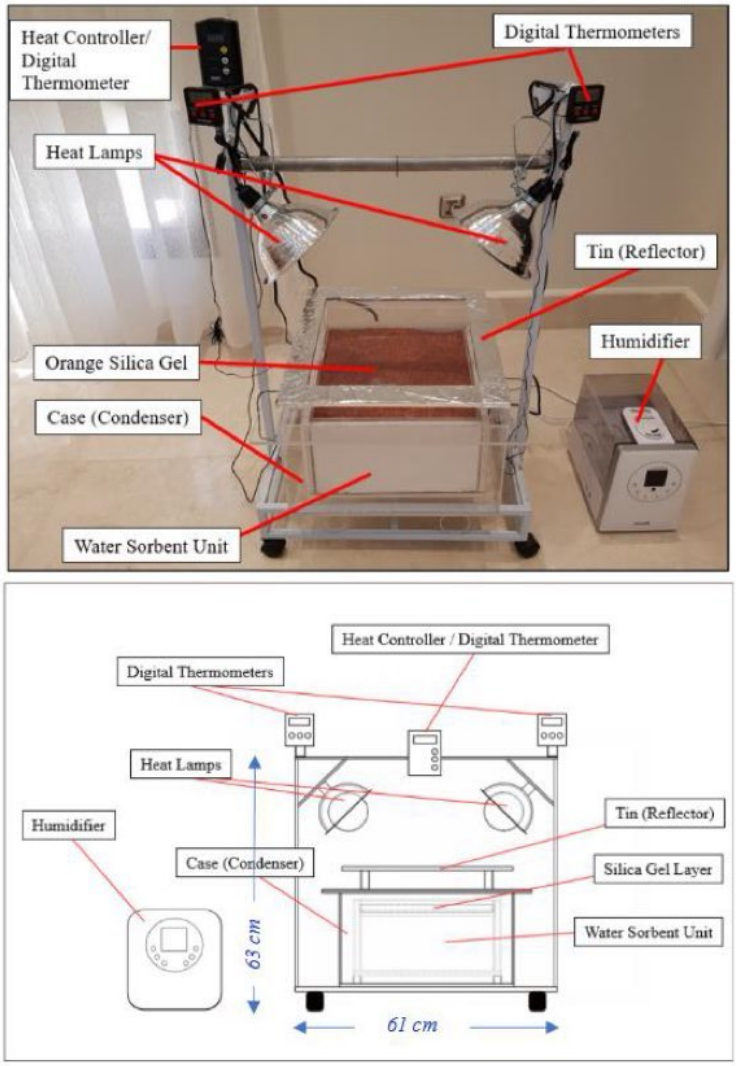

Figure 1.4: Water sorbent prototype and experimental setup [15].

1.4.2 Metal-Organic Frameworks

Metal-organic frameworks (MOFs) are highly porous materials with various potential water sorption mechanisms, making them promising for AWH. While challenges remain in their stability and precise control over sorption/desorption behaviors, customizing MOF structures and compositions can enhance their water harvesting performance (Table 1.1). Early examples, like MOF-801, have demonstrated efficient water capture even in low-humidity environments, aided by solar energy for desorption [7], [12].

Future research aims to improve MOF synthesis for large-scale water production, optimize sorption capacities under different conditions, and address stability and cycling issues, ultimately enhancing AWH efficiency and practicality [16]. Despite progress, challenges remain in enhancing MOF working capacities, understanding adsorption/desorption kinetics, ensuring stability, designing smart MOFs, and developing devices for improved performance in AWH systems [7].

Table 1.1: Comparison of currently promising research MOFs for AWH [7].

Adsorbent materials	Relative humidity %	Maximum water harvesting yield	System	References
MOF-801(Zr)	10–40 20	0.25 L/day 2.8 L	Air-cooled sorbent-based device, natural sunlight	[14], [17]
MOF-801(Zr)/G **MOF-303(Al)/G**	5–40	0.1 L/day 0.175 L/kg	Solar reflector	[18]
Cr-soc-MOF-1(Cr)	70	1.95 g/g	No external heat is needed (required lower RH)	[19]
Banasorb-22(Zn) **IRMOF1(Zn)**	- 	0.08 g/g 0.11 g/g	-	[20], [21]
Co2Cl2BTDD	5–30	0.82 g/g	-	[22]
LiCl@MIL-101(Cr)	30	0.77 g/g	Solar	[23]
UiO-66(Zr)	40	0.052 g/g	-	[24]
H2N-UiO-66(Zr)		0.038 g/g		
HSO3-UiO-66 (Zr)		0.068 g/g		
MIL-101(Cr)@GO	10–90	1.58 g/g	-	[25]

1.4.3 Passive atmospheric water harvesters

1.4.3.1 Fog collectors

One commonly known type of passive AWH is fog harvesters. They are devices that capture water droplets from fog and convert them into usable water. These devices typically consist of a mesh or net that collects the fog droplets funneled into a storage container (Figure 1.5) [11]. One of the main benefits of fog harvesters is that they can effectively capture water in areas with high humidity and frequent fog, making them particularly useful in coastal or mountainous regions. In addition, fog harvesters are relatively simple and low-cost devices, requiring minimal maintenance and energy inputs.

Various fog collector installations can be found globally, with notable examples in certain places such as the Namib Desert in Africa. The research was conducted in the area where fourteen Surface Fog Collectors (SFCs) were studied across three Topnaar villages in the Namib Desert. They recorded water collection rates of 2.122 liters per square meter in Klipneus village [9]. In another region, the Coquimbo region of Chile, during the 1980s, a research project involved the installation of fifty by forty meters square fog collectors to provide fresh water for 100 families [26]. From 1995 to 1999, large fog collectors were developed in Peru near Mejia town for reforestation and coastal ecosystem restoration [27], [28]. In Ecuador's Pachamama Grande, during 1995–97, 40 large Fog Collectors (LFCs) were constructed with collection efficiencies as high as 12 liters per square meter per day [15]. Similarly, a significant fog collector study was conducted in Oman during the 1990s, reporting daily average collection rates as high as 30 liters per square meter. However, considerable water collection only occurred during the two-month monsoon season,

limiting the usefulness of fog collectors in the region [29]. Additional fog collection projects worldwide are listed in Table 1.3 below.

Despite its potential benefits, fog harvesting faces several challenges and limitations. First, Fog harvesting is highly dependent on weather conditions, particularly fog [10], [30]. Therefore, they are only applicable in certain places with high fog frequency and intensity, which can impact the reliability of fog harvesters as a water source [11]. Second, Fog collectors require regular maintenance to ensure optimal performance [10]. Mesh or netting structures may become clogged with debris, reducing their efficiency in capturing water droplets. The quality of fog water collected by fog harvesters can vary depending on atmospheric conditions and the composition of fog [30]. High salt content or pollutants in fog water may necessitate treatment before it can be used for consumption or irrigation. However, ongoing research and technological advancements hold the potential to enhance the effectiveness and scalability of fog harvesting as a sustainable water source.

A

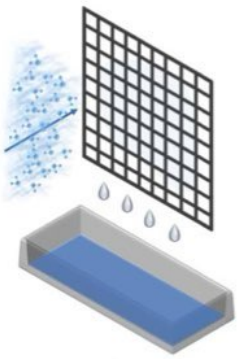

B

C

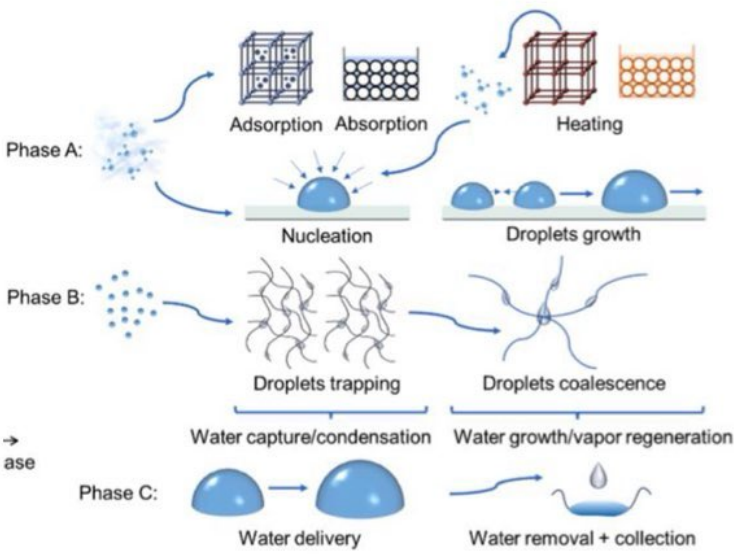

Figure 1.5: A) Schematic of a triangular mesh fog harvesting process positioned perpendicular to the wind. B) Image of a double-layered Raschel mesh. C) Water droplet evolution of a passive AWH fog collector from a phase-oriented perspective [26].

Table 1.2: Examples of current fog collector projects worldwide [26]

State/Country	Project	Year	Size/design/ cost	Type of application/issues	Water collection	Ref.
Falda Verde Mountain, Peru	Locally designed fog collector	1998–2001	1.5 m^2	-	100 l (day not stated)	[17]
Alto Patache, Chile	SFC fog collector	1987–2001	-	Primarily for ecosystem and climate research.	6 l per day	[17], [18]
Village of Tojquia in the Western Highlands	35 LFCs	2006–2012	-	High wind speeds are an issue.	Average of 6300 l of water per day in 4–6 months in winter dry season	[2]
Yemen (in the mountains near Hajja, inland from the Red Sea)	25 LFCs	2004	-	Stopped after a year due to insufficient community-level monitoring and issues related to occasional high wind speeds.	4.5 l m−2 per day over the 3-month dry winter period	[19]
Northwest of the island of Tenerife	Four LFCs were added in the 2000s, and four more were added in 2011.	The 2000s and 2011	-	The water is used for domestic purposes in the Forestry Commission Office, irrigation for the reforestation of endemic laurisilva species, and to prevent and fight against forest fires.	-	[20]
Lima, Peru	Project- 60 fog nets	2016	'Fog catchers' nylon nets designed. Cost: 500 USD per net	Supply free water to 250 households. The water is not drinkable and is thus used to sustain small-scale farming, wash clothes, and wash household utensils for low-income families.	100 l of water per day, saving almost 60% in water usage.	[21]
Tojquia, Guatemala	FogQuest project 35 large fog collectors (LFCs)	From 2006 to the present (2017)	40 square meters	For community use	Produces an average of about 200 l of water daily during the winter dry season.	[10]

1.4.3.2 Radiative Condensers

This type of AWH exploits the natural process of dissipating heat from a surface through long-wave radiation into the cold expanse of outer space via the atmospheric transparent window. Subsequently, it cools the ambient air below the dew point, facilitating water condensation, all without the need for external energy consumption [31], [32], [33]. As shown in Figure 1.6, unlike traditional cooling systems that require electricity or other energy sources, radiative condensers rely on natural processes such as thermal radiation and convection to effectively cool down equipment or processes [8]. However, radiative condensers depend on clear skies and low humidity for optimal performance [8], [34].In cloudy or humid conditions, the effectiveness of radiative cooling may be reduced, limiting their practical application in certain climates and regions. The maximum dew yield achievable by radiative condensers is limited to 0.8 L Day−1 m−2 based on the available radiative energy for condensation, with typical rates ranging between 25–100 W m−2 [58,63]. In practical applications, the maximum yield range is between 0.3–0.6 L day−1 m−2 [10]. Radiative condensers also require a larger footprint than traditional cooling systems, as they need open space to radiate heat into the atmosphere [34] effectively. This can be a challenge in urban or crowded environments with limited space.

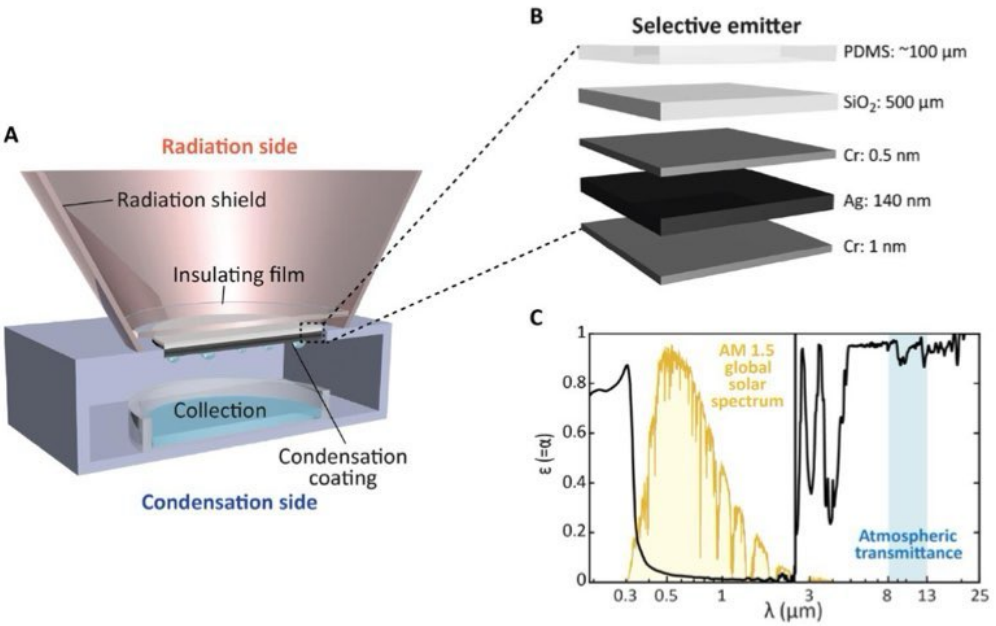

Figure 1.6: A) Working principle with separated radiation and condensation side. The radiation shield—optimized by accounting for the surrounding radiative environment—allows one to substantially improve the dew harvesting potential of the system and can be applied to any selective emitter. B) Structure of selective emitter. It consists of PDMS and silver, coated on a transparent glass substrate (chromium is used for oxidation protection and adhesion). C) Measured spectral absorptivity/emissivity of the selective emitter. The average emissivity in the atmospheric transparency window is very high, while the average absorptivity in the solar spectrum range is very low [6].

1.4.4 Thermoelectric Coolers

Thermoelectric coolers are innovative devices that transfer heat using the Peltier effect [35]. Unlike traditional refrigeration systems that rely on vapor compression, TECs operate on the principle of thermoelectricity, converting electrical energy into a thermal gradient. At the heart of a thermoelectric cooler lies the Seebeck effect, which states that a temperature difference across two dissimilar conductors generates an electric voltage [36]. In a TEC module, typically made of semiconductor materials like bismuth telluride (Bi2Te3), multiple pairs of p-type and n-type semiconductor elements are connected in series [37]. When a direct current (DC) is applied to the module, one side becomes hot while the other becomes cold, enabling heat transfer from one end to the other [35], as shown in Figure 1.7. Some advantages are that TECs are typically smaller and lighter than traditional refrigeration systems, making them suitable for compact applications [38].

TECs have no moving parts, resulting in quiet and vibration-free operation. TECs offer precise temperature control and can quickly switch between heating and cooling modes [36]. TECs do not use refrigerants like CFCs or HCFCs, reducing environmental impact. However, some limitations are that TECs are less efficient than traditional refrigeration systems and are best suited for low to moderate cooling loads. TECs can consume significant electrical power, especially at higher temperature differentials [39]. To maintain optimal performance, TECs require effective heat dissipation mechanisms, such as heat sinks and fans. A typical set-up is shown in Figure 1.8. TECs can be more expensive upfront than conventional cooling methods, although operational savings may offset this over time.

Table 1.3 shows a comparison table of different previously designed AWHs with TEC. The table summarizes the performance of all TEC prototypes and compares input and size parameters. The number of TEC modules used in each prototype is proportional to the total COP of the system. Each referenced design in Table 1.3 is carefully analyzed and considered in this prototype's mechanical design and optimization. A theoretical mathematical approach is introduced in the following chapter.

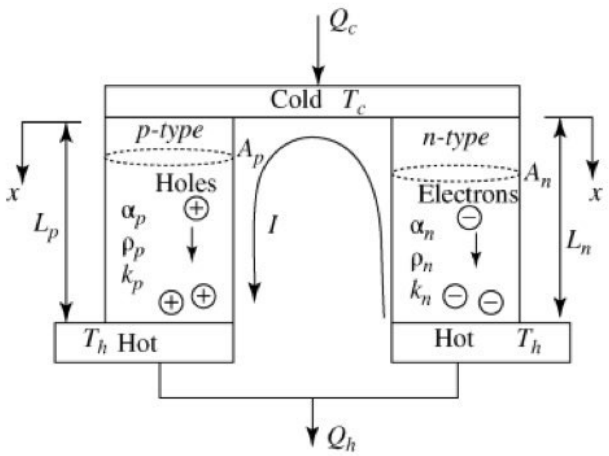

Figure 1.7: Thermoelectric cooler with p-type and n-type thermoelements

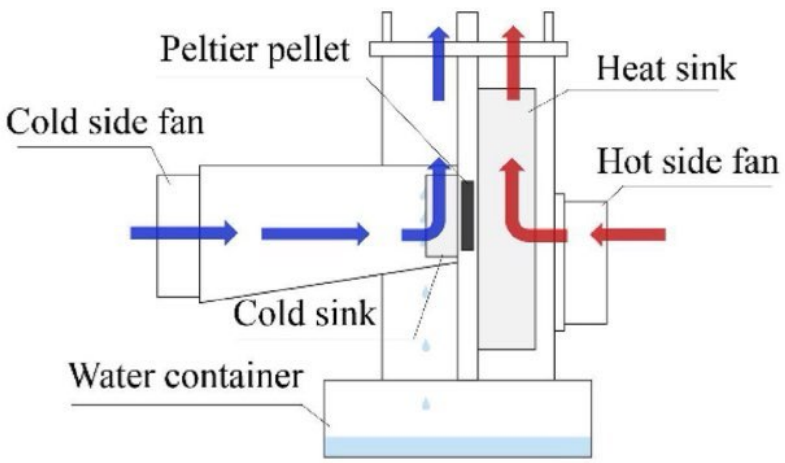

Figure 1.8: Schematic diagram of a TEC dehumidifying system.

Table 1.3: Comparison of TEC prototypes. [40]

S. No.	Author Name (Ref.)	Input Power (W)	Number of TECs	Cop
1	J.G Vian at al. [41]	100	3	0.8
2	C. Udomsakdigool et al. [42]	200-300W	2	0.88
3	Huajun and Chengying [43]	6	1	0.32
4	R.M. Atta [40]	120	3	-
5	M. Jradi et al. [44]	1000	20	1.52
6	C. Yildirim et al. [45]	140.26	1	0.78
7	V. P. Joshi et al. [46]	71	10	0.437
8	S. Liu et al. [47]	58.2	2	-
9	Yu Yao et al. [48]	-	4	0.75
10	C. Uttaslip et al. [49]	15	1	-
11	J. Kim et al. [50]	39.74	1	0.13
12	P. Rakkwamsuk et al. [51]	240	4	0.41
13	A. M. Shourideh et al. [39]	60-208	4	2

References

[1] M. Eslami, F. Tajeddini, and N. Etaati, "Thermal analysis and optimization of a system for water harvesting from humid air using thermoelectric coolers," *Energy Conversion and Management*, vol. 174, pp. 417–429, Oct. 2018, doi: 10.1016/j.enconman.2018.08.045.

[2] "Saving Water in Nevada".

[3] "Western Regional Climate Center." Accessed: May 09, 2024. [Online]. Available: https://wrcc.dri.edu

[4] C. Ingrao, R. Strippoli, G. Lagioia, and D. Huisingh, "Water scarcity in agriculture: An overview of causes, impacts and approaches for reducing the risks," *Heliyon*, vol. 9, no. 8, p. e18507, Jul. 2023, doi: 10.1016/j.heliyon.2023.e18507.

[5] M. A. Mohammad, A. J. Abid, and A. D. Farhood, "A Smart Embedded System for Humid Air Condensation and Water Harvesting," *IOP Conf. Ser.: Mater. Sci. Eng.*, vol. 881, no. 1, p. 012163, Jul. 2020, doi: 10.1088/1757-899X/881/1/012163.

[6] I. Haechler *et al.*, "Exploiting radiative cooling for uninterrupted 24-hour water harvesting from the atmosphere," *Sci Adv*, vol. 7, no. 26, p. eabf3978, Jun. 2021, doi: 10.1126/sciadv.abf3978.

[7] N. Asim *et al.*, "Sorbent-based air water-harvesting systems: progress, limitation, and consideration," *Rev Environ Sci Biotechnol*, vol. 20, no. 1, pp. 257–279, Mar. 2021, doi: 10.1007/s11157-020-09558-6.

[8] O. Clus, J. Ouazzani, M. Muselli, V. S. Nikolayev, G. Sharan, and D. Beysens, "Comparison of various radiation-cooled dew condensers using computational fluid dynamics," *Desalination*, vol. 249, no. 2, pp. 707–712, Dec. 2009, doi: 10.1016/j.desal.2009.01.033.

[9] V. Mtuleni, J. Henschel, and M. Seely, "Evaluation of fog-harvesting potential in Namibia," Jan. 1998.

[10] "Passive atmospheric water harvesting: Materials, devices, and perspectives - ScienceDirect." Accessed: Apr. 19, 2024. [Online]. Available: https://www.sciencedirect.com/science/article/pii/S2211285524003203

[11] H. Jarimi, R. Powell, and S. Riffat, "Review of sustainable methods for atmospheric water harvesting," *International Journal of Low-Carbon Technologies*, vol. 15, no. 2, pp. 253–276, May 2020, doi: 10.1093/ijlct/ctz072.

[12] X. Zhou, H. Lu, F. Zhao, and G. Yu, "Atmospheric Water Harvesting: A Review of Material and Structural Designs," *ACS Materials Lett.*, vol. 2, no. 7, pp. 671–684, Jul. 2020, doi: 10.1021/acsmaterialslett.0c00130.

[13] A. LaPotin *et al.*, "Dual-Stage Atmospheric Water Harvesting Device for Scalable Solar-Driven Water Production," *Joule*, vol. 5, no. 1, pp. 166–182, Jan. 2021, doi: 10.1016/j.joule.2020.09.008.

[14] H. Kim *et al.*, "Adsorption-based atmospheric water harvesting device for arid climates," *Nat Commun*, vol. 9, no. 1, p. 1191, Mar. 2018, doi: 10.1038/s41467-018-03162-7.

[15] A. K. Sleiti, H. Al-Khawaja, H. Al-Khawaja, and M. Al-Ali, "Harvesting water from air using adsorption material – Prototype and experimental results," *Separation and Purification Technology*, vol. 257, p. 117921, Feb. 2021, doi: 10.1016/j.seppur.2020.117921.

[16] M. W. Logan, S. Langevin, and Z. Xia, "Reversible Atmospheric Water Harvesting Using Metal-Organic Frameworks," *Sci Rep*, vol. 10, no. 1, p. 1492, Jan. 2020, doi: 10.1038/s41598-020-58405-9.
[17] H. Kim *et al.*, "Water harvesting from air with metal-organic frameworks powered by natural sunlight," *Science*, vol. 356, no. 6336, pp. 430–434, Apr. 2017, doi: 10.1126/science.aam8743.
[18] F. Fathieh, M. J. Kalmutzki, E. A. Kapustin, P. J. Waller, J. Yang, and O. M. Yaghi, "Practical water production from desert air," *Science Advances*, vol. 4, no. 6, p. eaat3198, Jun. 2018, doi: 10.1126/sciadv.aat3198.
[19] S. M. Towsif Abtab *et al.*, "Reticular Chemistry in Action: A Hydrolytically Stable MOF Capturing Twice Its Weight in Adsorbed Water," *Chem*, vol. 4, no. 1, pp. 94–105, Jan. 2018, doi: 10.1016/j.chempr.2017.11.005.
[20] N. L. Rosi *et al.*, "Hydrogen Storage in Microporous Metal-Organic Frameworks," *Science*, vol. 300, no. 5622, pp. 1127–1129, May 2003, doi: 10.1126/science.1083440.
[21] T. Wu *et al.*, "Enhancing the stability of metal-organic frameworks in humid air by incorporating water repellent functional groups," *Chem Commun (Camb)*, vol. 46, no. 33, pp. 6120–6122, Sep. 2010, doi: 10.1039/c0cc01170c.
[22] A. J. Rieth, S. Yang, E. N. Wang, and M. Dincă, "Record Atmospheric Fresh Water Capture and Heat Transfer with a Material Operating at the Water Uptake Reversibility Limit," *ACS Cent. Sci.*, vol. 3, no. 6, pp. 668–672, Jun. 2017, doi: 10.1021/acscentsci.7b00186.
[23] J. Xu *et al.*, "Efficient Solar-Driven Water Harvesting from Arid Air with Metal-Organic Frameworks Modified by Hygroscopic Salt," *Angew Chem Int Ed Engl*, vol. 59, no. 13, pp. 5202–5210, Mar. 2020, doi: 10.1002/anie.201915170.
[24] F. Trapani, A. Polyzoidis, S. Loebbecke, and C. G. Piscopo, "On the general water harvesting capability of metal-organic frameworks under well-defined climatic conditions," *Microporous and Mesoporous Materials*, vol. 230, pp. 20–24, Aug. 2016, doi: 10.1016/j.micromeso.2016.04.040.
[25] J. Yan *et al.*, "Adsorption isotherms and kinetics of water vapor on novel adsorbents MIL-101(Cr)@GO with super-high capacity," *Applied Thermal Engineering*, vol. 84, pp. 118–125, Jun. 2015, doi: 10.1016/j.applthermaleng.2015.03.040.
[26] R. S. Schemenauer, H. Fuenzalida, and P. Cereceda, "A Neglected Water Resource: The Camanchaca of South America," *Bulletin of the American Meteorological Society*, vol. 69, no. 2, pp. 138–147, Feb. 1988, doi: 10.1175/1520-0477(1988)069<0138:ANWRTC>2.0.CO;2.
[27] F. Salbitano *et al.*, "Dynamics and evolution of tree populations and soil-vegetation relationships in Fogscapes: Observations over a period of 14 years at the experimental sites of Meija (Peru)," Jul. 2010.
[28] R. S. Schemenauer and P. Cereceda, "Meteorological conditions at a coastal fog collection site in Peru," *Atmósfera*, vol. 6, no. 3, Art. no. 3, 1993, Accessed: Apr. 20, 2024. [Online]. Available: https://www.revistascca.unam.mx/atm/index.php/atm/article/view/8354

[29] R. S. Schemenauer and P. Cereceda, “Monsoon cloudwater chemistry on the Arabian Peninsula,” *Atmospheric Environment. Part A. General Topics*, vol. 26, no. 9, pp. 1583–1587, Jun. 1992, doi: 10.1016/0960-1686(92)90058-S.
[30] X. Liu, D. Beysens, and T. Bourouina, “Water Harvesting from Air: Current Passive Approaches and Outlook,” *ACS Materials Lett.*, vol. 4, no. 5, pp. 1003–1024, May 2022, doi: 10.1021/acsmaterialslett.1c00850.
[31] C. Y. Tso, K. C. Chan, and C. Y. H. Chao, “A field investigation of passive radiative cooling under Hong Kong’s climate,” *Renewable Energy*, vol. 106, pp. 52–61, Jun. 2017, doi: 10.1016/j.renene.2017.01.018.
[32] X. Sun, Y. Sun, Z. Zhou, M. A. Alam, and P. Bermel, “Radiative sky cooling: fundamental physics, materials, structures, and applications,” *Nanophotonics*, vol. 6, no. 5, pp. 997–1015, Sep. 2017, doi: 10.1515/nanoph-2017-0020.
[33] E. A. Goldstein, A. P. Raman, and S. Fan, “Sub-ambient non-evaporative fluid cooling with the sky,” *Nat Energy*, vol. 2, no. 9, pp. 1–7, Sep. 2017, doi: 10.1038/nenergy.2017.143.
[34] G. Sharan, “Harvesting Dew with Radiation Cooled Condensers to Supplement Drinking Water Supply in Semi-arid Coastal Northwest India,” *International Journal for Service Learning in Engineering*, vol. 6, pp. 132–152, May 2011, doi: 10.24908/ijsle.v6i1.3188.
[35] R. M. Atta, “Solar Water Condensation Using Thermoelectric Coolers,” 2011.
[36] H. Lee, “Thermoelectrics Thermoelectrics Design and Materials,” Jan. 2016, Accessed: Apr. 20, 2024. [Online]. Available: https://www.academia.edu/73566131/Thermoelectrics_Thermoelectrics_Design_and_Materials
[37] P. A. Finn, C. Asker, K. Wan, E. Bilotti, O. Fenwick, and C. B. Nielsen, “Thermoelectric Materials: Current Status and Future Challenges,” *Front. Electron. Mater*, vol. 1, Aug. 2021, doi: 10.3389/femat.2021.677845.
[38] T. J. Kadhim, A. K. Abbas, and H. J. Kadhim, “Experimental study of atmospheric water collection powered by solar energy using the Peltier effect,” *IOP Conf. Ser.: Mater. Sci. Eng.*, vol. 671, no. 1, p. 012155, Jan. 2020, doi: 10.1088/1757-899X/671/1/012155.
[39] A. H. Shourideh, W. Bou Ajram, J. Al Lami, S. Haggag, and A. Mansouri, “A comprehensive study of an atmospheric water generator using Peltier effect,” *Thermal Science and Engineering Progress*, vol. 6, pp. 14–26, Jun. 2018, doi: 10.1016/j.tsep.2018.02.015.
[40] R. S. Srivastava, A. Kumar, S. Sharma, H. Thakur, S. Patel, and R. Vaish, “Development and applications of thermoelectric based dehumidifiers,” *Energy and Buildings*, vol. 252, p. 111446, Dec. 2021, doi: 10.1016/j.enbuild.2021.111446.
[41] J. G. Vián, D. Astrain, and M. Domínguez, “Numerical modelling and a design of a thermoelectric dehumidifier,” *Applied Thermal Engineering*, vol. 22, no. 4, pp. 407–422, Mar. 2002, doi: 10.1016/S1359-4311(01)00102-8.
[42] C. Udomsakdigool, J. Hirunlabh, J. Khedari, and B. Zeghmati, “Design Optimization of a New Hot Heat Sink with a Rectangular Fin Array for Thermoelectric Dehumidifiers,” *Heat Transfer Engineering*, vol. 28, no. 7, pp. 645–655, Jul. 2007, doi: 10.1080/01457630701266470.

[43] W. Huajun and Q. Chengying, “Experimental study of operation performance of a low power thermoelectric cooling dehumidifier”.
[44] M. Jradi, N. Ghaddar, and K. Ghali, “Experimental and theoretical study of an integrated thermoelectric–photovoltaic system for air dehumidification and fresh water production,” *International Journal of Energy Research*, vol. 36, no. 9, pp. 963–974, 2012, doi: 10.1002/er.1848.
[45] C. Yıldırım, S. K. Soylu, İ. Atmaca, and İ. Solmuş, “Experimental investigation of a portable desalination unit configured by a thermoelectric cooler,” *Energy Conversion and Management*, vol. 85, pp. 140–145, Sep. 2014, doi: 10.1016/j.enconman.2014.05.071.
[46] V. P. Joshi, V. S. Joshi, H. A. Kothari, M. D. Mahajan, M. B. Chaudhari, and K. D. Sant, “Experimental Investigations on a Portable Fresh Water Generator Using a Thermoelectric Cooler,” *Energy Procedia*, vol. 109, pp. 161–166, Mar. 2017, doi: 10.1016/j.egypro.2017.03.085.
[47] S. Liu *et al.*, “Experimental analysis of a portable atmospheric water generator by thermoelectric cooling method,” *Energy Procedia*, vol. 142, pp. 1609–1614, Dec. 2017, doi: 10.1016/j.egypro.2017.12.538.
[48] Y. Yao *et al.*, “Optimization design and experimental study of thermoelectric dehumidifier,” *Applied Thermal Engineering*, vol. 123, pp. 820–829, Aug. 2017, doi: 10.1016/j.applthermaleng.2017.05.172.
[49] C. Uttasilp, N. Patcharaprakiti, T. Somsak, and J. Thongpron, “Optimal solar energy on thermoelectric cooler of water generator in case study on flood crisis,” *Jpn. J. Appl. Phys.*, vol. 57, no. 8S3, p. 08RH05, Jul. 2018, doi: 10.7567/JJAP.57.08RH05.
[50] J. Kim, K. Park, D.-G. Lee, Y. S. Chang, and H.-Y. Kim, “Optimal cold sink temperature for thermoelectric dehumidifiers,” *J Mech Sci Technol*, vol. 32, no. 2, pp. 885–895, Feb. 2018, doi: 10.1007/s12206-018-0139-8.
[51] P. Rakkwamsuk, P. Paromupatham, K. Sathapornprasath, C. Lertsatitthanakorn, and S. Soponronnarit, “An experimental investigation on the performance of a thermoelectric dehumidification system,” *Journal of Mechanical Engineering and Sciences*, vol. 12, pp. 4117–4126, Dec. 2018, doi: 10.15282/jmes.12.4.2018.10.0356.
[52] D. Zhao and G. Tan, “A review of thermoelectric cooling: Materials, modeling and applications,” *Applied Thermal Engineering*, vol. 66, no. 1, pp. 15–24, May 2014, doi: 10.1016/j.applthermaleng.2014.01.074.
[53] V. Patel, R. Patel, and J. Patel, “Theoretical and experimental investigation of bubble column humidification and thermoelectric cooler dehumidification water desalination system,” *International Journal of Energy Research*, vol. 44, no. 2, pp. 890–901, 2020, doi: 10.1002/er.4931.
[54] G. Tang, S. M. Rabeek, and M. A. Arasu, “Thermal design and temperature gradient analysis for a thermoelectric energy harvest device in off-shore and marine application,” in *2016 IEEE 18th Electronics Packaging Technology Conference (EPTC)*, Nov. 2016, pp. 648–652. doi: 10.1109/EPTC.2016.7861560.
[55] K. Almutairi, K. Irshad, S. Algarni, A. Ali, and S. Islam, “Experimental investigation of dehumidification process regulated by the photothermoelectric

system," *Water Sci Technol*, vol. 84, no. 10–11, pp. 3211–3226, Nov. 2021, doi: 10.2166/wst.2021.368.

[56] M. A. Muñoz-García, G. P. Moreda, M. P. Raga-Arroyo, and O. Marín-González, "Water harvesting for young trees using Peltier modules powered by photovoltaic solar energy," *Computers and Electronics in Agriculture*, vol. 93, pp. 60–67, Apr. 2013, doi: 10.1016/j.compag.2013.01.014.

[57] A. Alenezi and H.-H. Jung, "Design and preliminary experimental testing of a water harvester using the Peltier effect," *jkosme*, vol. 42, no. 5, pp. 358–363, Jun. 2018, doi: 10.5916/jkosme.2018.42.5.358.

CHAPTER 2: MODELING, DESIGN AND OPTIMAZATION OF A SINGLE THERMOELECTRIC MODULE

1. Theoretical Mathematical Modeling of a Single Module

Each thermoelectric cooling module is unique by four main characteristics. They are the maximum current I_{max} in amps (A), the maximum voltage V_{max} in voltage (V), the maximum temperature difference ΔT_{max} in (K), and the maximum heat dissipation Q_{max} in (W). Such parameters can be utilized to identify three important characteristics of the Peltier module, which are the Seebeck coefficient of the module S_m in volts per kelvin $\left(\frac{V}{K}\right)$, the electrical resistivity of the module R_m in ohms (Ω), and the thermal conductivity of the module K_m in watts per kelvin $\left(\frac{W}{K}\right)$. Each of the predefined characteristics is dependent on the hot side temperature of the Peltier module, which is a variable Th in degrees kelvin (K) [1], [2], [3], [4].

$$S_m = \frac{V_{max}}{Th} \tag{1}$$

$$R_m = \frac{(Th-\Delta T_{max})V_{max}}{Th \times I_{max}} \tag{2}$$

$$K_m = \frac{(Th-\Delta T_{max})V_{max}I_{max}}{2Th\Delta T_{max}} \tag{3}$$

Each one of the previously defined characteristics Eqns. 1 to 3 are applied in the energy balance Eqns. 4 to 6 for a single TEC module to solve for the heat absorption rate Q_c, the heat dissipation rate Q_h, and the TEC module power consumption P_{TEC} in watts (W). Eqns. 4 to 6 are a function of the input electric current I in amps (A) [5].

$$Q_c = SmIT_c - \frac{1}{2}I^2R_m + K_m(T_h - T_c) \tag{4}$$

$$Q_h = SmIT_h + \frac{1}{2}I^2R_m + K_m(T_h - T_c) \tag{5}$$

$$P_{TEC} = SmI(T_h - T_c) + \frac{1}{2}I^2R_m \tag{6}$$

Eqn. 6 can also be written as a function of the heat dissipation rate minus the heat absorption rate of the TEC module, according to the first law of thermodynamics. The difference between the hot surface temperature Th in degrees kelvin (K) minus the cold surface temperature Tc in degrees kelvin (K) can be expressed as shown in Eqn. 8 in degrees kelvin (K).

$$P_{TEC} = Q_h - Q_c \tag{7}$$

$$\Delta T = Th - Tc \tag{8}$$

The coefficient of performance of the TEC (unitless), is expressed as a function of the heat absorption rate Q_c in Eqn. 7.

$$COP = \frac{Q_c}{P_{TEC}} \tag{9}$$

Theoretically, the AHW comprises six TECs in series in a long channel. The width of the channel $w_{channel}$ is 63mm, and each TEC module is placed 1.5cm apart. Heat sinks are placed on both sides of the TECs to increase the surface area and the surface heat transfer of the system, making a long channel on both sides of the TECs in series. The entering air stream passes through the channel on which the cold side of the TECs are placed. A fan supplies the required airflow circulation. The temperature distribution on the surface of the channel on both sides of the TECs is assumed to be uniform. Figure 2.1 shows the conceptual schematic of the system, heatsink dimensions, and airflow direction. The layout of a single fin of the heat sinks is shown in Figure 2.2.

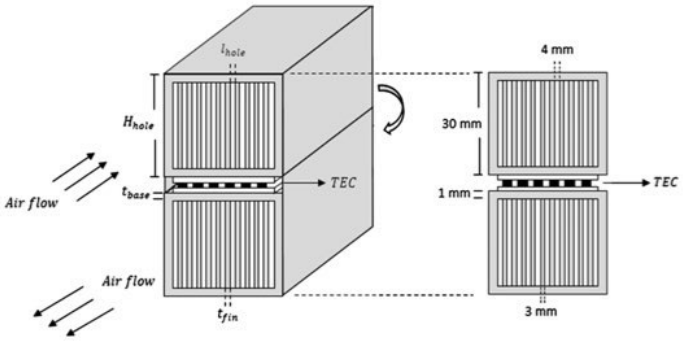

Figure 2.1: Schematic of the system. Figure adapted from Thermal analysis and optimization of a system for water harvesting from humid air using thermoelectric coolers [3]

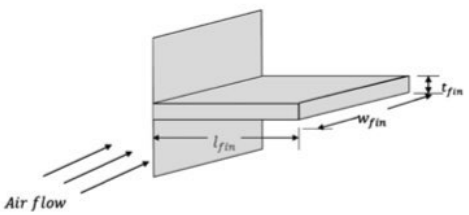

Figure 2.2: Layout of a single heatsink fin. Figure adapted from Thermal analysis and optimization of a system for water harvesting from humid air using thermoelectric coolers [3]

The heat transfer between the air and the TECs in the cold channel is related to the enthalpy change as follows:

$$Q_c = \dot{m}_c(h_{air-in-c} - h_{air-out-c}) \quad (10)$$

where C_p the specific heat of the air in joules per kilogram of kelvin $\left(\frac{J}{Kg \times K}\right)$ and h the enthalpy, the entering and exiting humid air in $\left(\frac{J}{Kg}\right)$ as a function of specific humidity ω in kilograms per kilograms $\left(\frac{Kg}{Kg}\right)$. The enthalpy of humid air can be calculated using Eqn. 11, where T is the temperature of the inlet or outlet air in the cold channel [44].

$$h = C_p(T - 273) + \omega\big(2501.3 + 1.86(T - 273)\big) * 1000 \quad (11)$$

As no water condensation occurs in the hot channel, the air's specific humidity does not change, so the enthalpy changes can be replaced by the air's specific heat, which changes the inlet and outlet temperatures. In addition, since the hot side of the TECs is exposed and cooled by ambient air, the inlet hot side temperature is equal to the outlet cold side temperature. $T_{air-in-h} = T_a$. Therefore, the heat transfer between the air and the hot channel is expressed as follows:

$$Q_h = \dot{m}_c C_p (T_{air-out-h} - T_a) \quad (12)$$

The heat transfer in the channels is also related to the temperature difference between the air stream and the hot and cold surfaces as follows:

$$Q_c = \frac{\left\{\frac{[(T_{air-out-c} - T_c) - (T_a - T_c)]}{\ln\left(\frac{T_{air-out-c} - T_c}{T_a - T_c}\right)}\right\}}{Rc} \quad (13)$$

$$Q_h = \frac{\left\{\frac{[(T_h - T_a) - (T_h - T_{air-out-h})]}{\ln\left(\frac{T_h - T_a}{T_h - T_{air-out-h}}\right)}\right\}}{Rh} \quad (14)$$

In Eqns. 13 and 14, Rc and Rh are the total thermal resistances between the TEC surface in ohms () and the airflow in the cold and hot channels, respectively. Rc and Rh can be calculated by adding the different thermal resistances shown in Fig. 2.3.

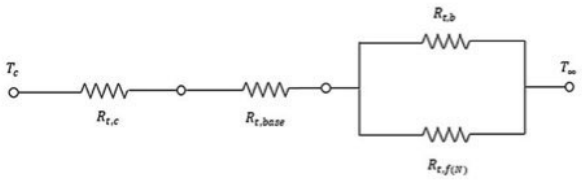

Figure 2.3: Thermal resistances between the cold side of the TEC and airflow in the channel. Figure adapted from Thermal analysis and optimization of a system for water harvesting from humid air using thermoelectric coolers [3]

In Figure 2.3 $R_{t,c}$ the contact resistance between the TECs and the heat sinks attached to the cold channel. It can be modeled using the following expression:

$$R_{t,c} = \frac{R"_{t,c}}{N_{TEC} l_{TEC} W_{TEC}} \tag{15}$$

where N_{TEC} is the number of TECs, l_{TEC} is the length of the TEC and W_{TEC} is the width of the TEC. $R_{t,base}$ is the thermal resistance of the base surface on which the TECs are installed and is calculated as follows:

$$R_{t,base} = \frac{t_{base}}{k_s \times l_{channel} \times w_{channel}} \tag{16}$$

where t_{base}, $l_{channel}$ and $w_{channel}$ are the baste's thickness, the channel's length, and the channel's width. Ks is the thermal conductivity of the base plate material in watts per meter square times kelvin $\left(\frac{W}{m^2 \times K}\right)$. The convection heat transfer resistance of the un-finned part of the heat sink $R_{t,b}$ can be combined with the resistance of the extended surface $R_{t,f(N)}$ as an equivalent resistance R_{equ} in ohms (Ω).

$$R_{equ} = \frac{1}{n_0 \times A_t \times h_{conv}} \tag{17}$$

The overall efficiency of the heat sink is given by:

$$n_0 = 1 - \frac{N_{fin}A_f}{A_t}(1 - n_f) \quad (18)$$

$$A_f = 2w_{fin}l_c \quad (19)$$

$$l_c = l_{fin} + \frac{t_{fin}}{2} \quad (20)$$

$$A_t = l_{hole}l_{channel}N_{hole} + (2N_{hole} - 2)H_{hole}l_{channel} \quad (21)$$

where N_{fin}, A_f, A_t, l_c and N_{hole} are the number of fins, the fin area, the total area of heat transfer, the equivalent in length, and the number of air passages, respectively. Also, H_{hole} and l_{hole} are the height and length of the fin separation hole. l_{fin}, w_{fin} and t_{fin} are the fins' length, width, and thickness [41].

Assuming that the fin tips are adiabatic, n_f is given by:

$$n_f = \frac{tanh \times m \times l_c}{m \times l_c} \quad (22)$$

$$m = \sqrt{\frac{h_{conv} \times p}{k_s \times A_c}} \quad (25)$$

$$p = 2(w_{fin} + t_{fin}) \quad (26)$$

$$A_c = w_{fin} \times t_{fin} \quad (27)$$

where p is the perimeter, and A_c is the cross-section area of a rectangular fin.

The convection heat transfer coefficient h_{conv} (in watts per meter square times kelvin $\frac{W}{m^2 \times K}$) is calculated from the Nusselt number shown below:

$$h_{conv} = \frac{Nuk_f}{D_{hyd}} \quad (28)$$

where k_f is the thermal conductivity of air and D_{hyd} is the hydraulic diameter of the heatsinks. Assuming turbulent flow for both cooling and heating channels:

$$Nu = 0.023Re^{0.8}Pr^{0.3}\ for\ cooling \tag{29}$$

$$Nu = 0.023Re^{0.8}Pr^{0.4}\ for\ heating \tag{30}$$

where Pr is the Prandtl number, and Re is the Reynolds number defined as follows:

$$Re = \frac{u_{average} \times D_{hyd}}{v} \tag{31}$$

$$u_{average} = \frac{\frac{\dot{m}_a}{N_{hole}}}{\rho \times l_{hole} \times H_{hole}} \tag{32}$$

where v is the kinematic viscosity of the hot/cold channel in meters square per seconds $\left(\frac{m^2}{s}\right)$, ρ is the density of ambient air in kilograms per meter cube $\left(\frac{kg}{m^3}\right)$, $\dot{m}_a$ is the total mass flow rate of airflow (assuming which is constant throughout the entire hot/cold channels) in kilograms per second $\left(\frac{kg}{s}\right)$. The characteristic length is the hydraulic diameter given by:

$$D_{hyd} = \frac{4 l_{hole} H_{hole}}{2(l_{hole} + H_{hole})} \tag{33}$$

The total resistance is obtained by:

$$R = R_{t,c} + R_{t,base} + R_{equ} \tag{34}$$

The same procedure is performed for both hot and cold side channels to get Rh, Rc, $h_{conv,hot}$, $h_{conv,cold}$, Re_{cold}, Re_{hot}, Nu_{hot} and Nu_{cold}. The volume flow rate of water production in liters per second $\left(\frac{L}{s}\right)$ is obtained using the following mass balance equation for water: the density of water ($\rho_{average}$) is also shown below in (kg/s):

$$\dot{V}_w = \dot{m}_a(\omega_{air-in-c} - \omega_{air-out-c})\left(\frac{1000}{\rho_{average}}\right) \tag{35}$$

$$\rho_{average} = \frac{T_{air-out-c} - T_{air-in-c}}{2} \tag{36}$$

To calculate the required fan power, the pressure drops ($\Delta\rho$) in Pascals (Pa) across the air passage is required, and the friction factor:

$$\Delta p = \frac{f(\rho u_{average}^2)}{D_{hyd}} l_{channel} \quad (37)$$

$$f = (0.790 \ln(Re) - 1.64)^{-2} \quad (38)$$

The fan power consumption is given by:

$$P_{fan} = \frac{\dot{m}}{\rho} \Delta p \quad (39)$$

2. Theoretical Modeling Parameters of a Single Module

The following theoretical model was utilized as a reference point to predict the thermoelectric module behavior. The thermophysical properties of air are considered for typical Reno weather conditions of 298K (25℃) and a fixed relative humidity of 20%. By implementing such parameters from the start, one can identify the minimum number of TECs and heat sinks necessary for the system to condense a minimum of one liter of water per day.

Table 2.1: Fixed Thermophysical Properties of Air. Parameters are taken from multiple referenced sources.

Thermophysical Properties of Air	
Ambient temperature (K)	298K
Relative humidity (%)	20%
Humidity ratio (kg/kg)	0.003931 kg/kg
Cold channel mass flow rate (kg/s)	0.02736 kg/s
Hot channel Mass flow rate (kg/s)	0.08158 kg/s
Cold channel specific heat (J/ (kg K))	1004 J/ (kg K)
Hot channel specific heat (J/ (kg K))	1006 J/ (kg K)
Cold channel air density (kg/m^3)	1.341 kg/m^3
Hot channel air density (kg/m^3)	1.246 kg/m^3
Thermal conductivity of base airflow in the cold channel (W / (m K))	0.02288 W / (m K)
Thermal conductivity of base airflow in the hot channel (W / (m K))	0.02439 W / (m K)
Thermal conductivity of base plate material (W / (m K))	180 W / (m K)
Kinematic Viscosity of cold channel (m^2/s)	12.52E-06
Kinematic Viscosity of hot channel (m^2/s)	14.26E-06
Prandtl number of cold channels	0.7387
Prandtl number of hot channels	0.7336

Table 2.2: Heat sink dimensions.

Heat Sink Parameters (m)	
Length of the channel hole (lhole)	0.9E-3
Height of the channel hole (Hhole)	3.7E-2
Number of the channel holes (Nhole)	10
Thickness of the Base (tbase)	0.4E-2
Thickness of the Fin (tfin)	1E-3
Number of Fins (Nfin)	9
Length of the TEC's Channel (lchannel)	14.5E-2
Width of the TEC's Channel (wchannel)	10.1E-2
Width of the Fins (wfin)	14E-2
Length of the Fins (lfin)	37E-2

Table 2.3: Thermoelectric cooler fixed parameters.

TEC Parameters (CP4055485)	
Maximum Current (Imax)	4A
Maximum Voltage (Vmax)	15.4V
Maximum Temperature Difference (ΔTmax)	70K
Length of the TEC's (ltec)	44E-3
Width of the TECs (wtec)	44E-3
Number of TEC's (NTEC)	1-8

3. Theoretically Modeling Results of a Single Module

The following simulations are performed under the previously shown typical weather conditions in Reno, NV. The ambient temperature is 298K (25°C) and the relative humidity is 20%. The mass flow rate of the cold/hot side of the system is 0.02736 kg/s and 0.08158 kg/s (airflow 45CFM/134CFM). As shown in Fig. 2.4, the maximum predicted quantity of water a single module can condense in one hour is 4.5 ml/h with two TECs. Figures 2.5 to 2.12 show the predicted cold/hot side average temperatures, power consumption, temperature range, heat absorption rate, heat dissipation rate, coefficient of performance, and efficiency for a single module implementing the previously discussed parameters.

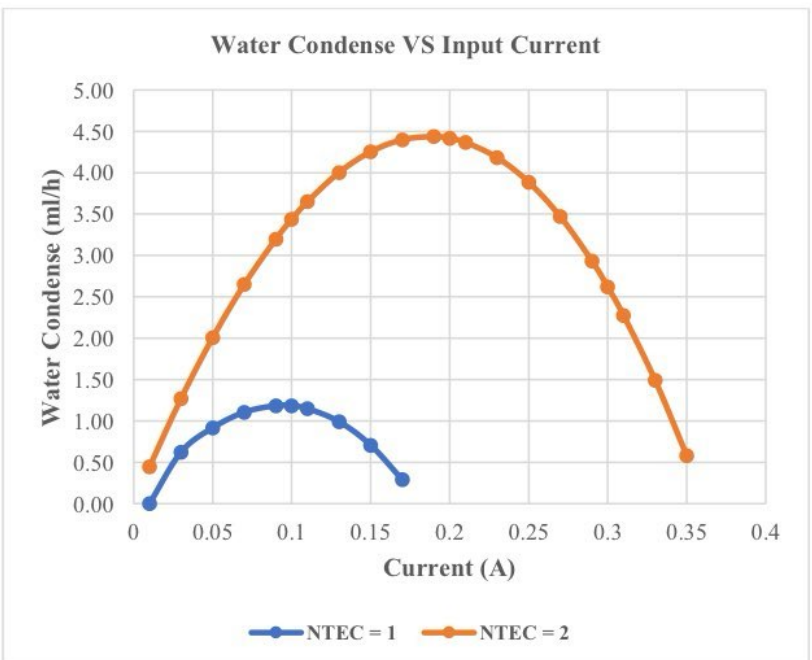

Figure 2.4: Water Condensed VS Input Current. These simulations are for the previously discussed module parameters.

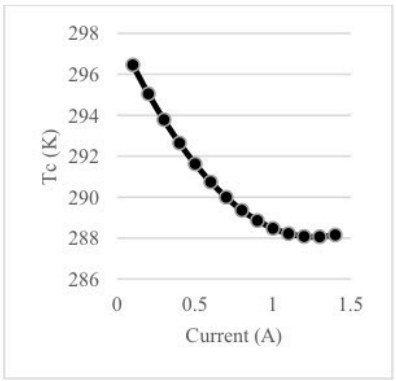

Figure 2.5: Predicted Cold side temperature distribution of a single module with two TECs.

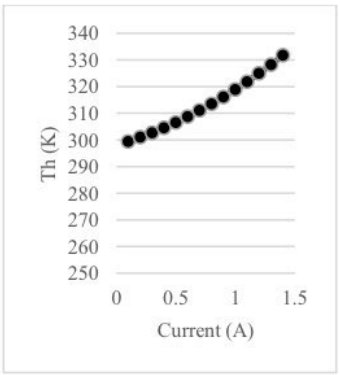

Figure 2.6: Predicted Hot temperature distribution of a single module with two TECSs.

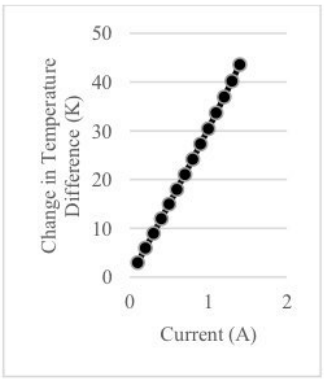

Figure 2.7: Predicted Temperature difference of a single module with two TECs.

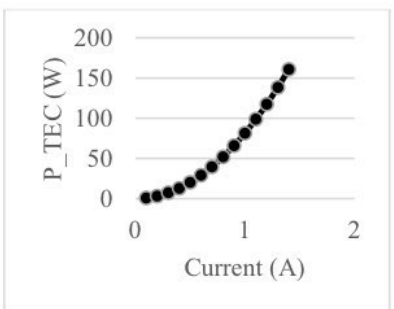

Figure 2.8 Predicted input power of the module with two TECs.

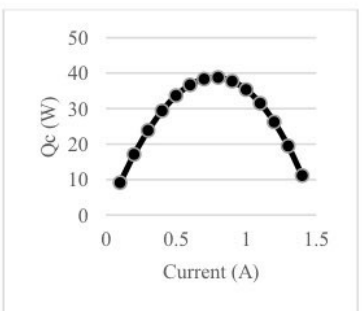

Figure 2.9: Predicted heat removal from the module's cold side with two TECs.

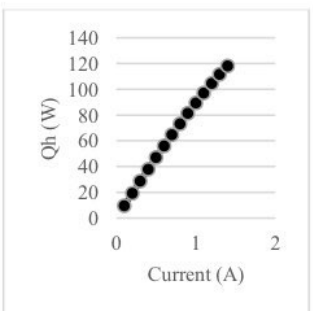

Figure 2.10: Predicted heat removal from the module's hot side with two TECs.

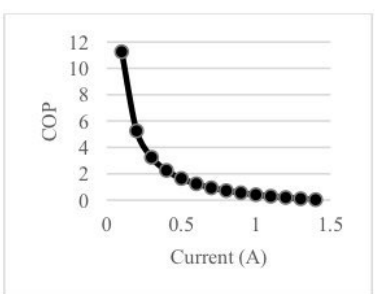

Figure 2.11: Predicted changes in the Coefficient of Performance of the module with two TECs.

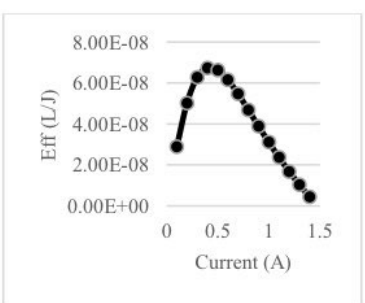

Figure 2.12: Predicted efficiency of the module with two TECs.

4. Single Module Operational Design

4.1 Electronics Design

The AWH is controlled by three circuits: the TEC's diving circuit, the temperature driving circuit, and the humidity driving circuit. Each section is independent but shares the same 12V potential to utilize a single power source to reduce total power consumption. The TEC's driving circuit mainly comprises n-channel metal-oxide-semiconductor field effect transistors (MOSFETs). The principle modulates the input gate voltage so that each transistor acts as an automated switch, controlling the current flow from the drain to the source, thus allowing the TEC's input power to be. The gate is controlled by a pulse width modulating signal (PWM) with a magnitude of 0-5V digitally generated by a USB-6212 National Instruments DAQ card and controlled by a designed LabVIEW software.

The temperature circuit uses precision thermocouple amplifiers with cold junction compensation. It reads the slight change in current from a K-type thermocouple, which is proportional to a change in temperature. The software reads the current output from the amplifier and easily converts the current to temperature in degrees Celsius. Each amplifier is rated at 5V input voltage and reads the output of a single thermocouple. Therefore, the fixed 12V potential of the circuit is regulated to 5V, and there are seven thermocouples in total. The humidity sensing circuits are designed to control three HIH-4000 Series Humidity sensors. The principle of each circuit design is shown in Figure 2.13

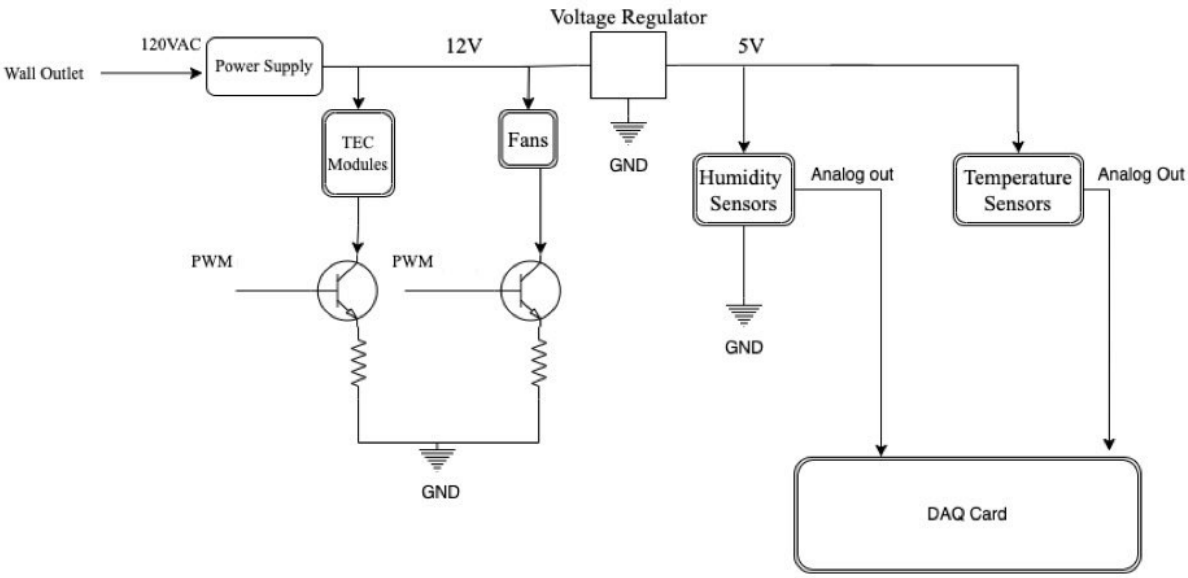

Figure 2.13: Overall Electronics Design Schematic

4.1.1 TEC Control Driving Circuit

To drive the TEC's six automotive N-Channel 60V (D-S) 175℃ MOSFETs are used. The gate-to-source voltage is modulated from 0 to 5 V by a PWM signal digitally generated by LabVIEW 2020 software with a frequency of 1Hz. Each MOSFET's potential drain to source voltage is fixed at 12V and 4.5A. Each MOSFET controls a single TEC, but six gates of the MOSFET are synchronized to a single PWM signal.

4.1.2 Fan Control Driving Circuit

The same kind of MOSFETs are used to drive the fans. The prototype has four 127 by 127 by 38 mm DC fans. Three fans are bolted on the top of the heatsinks and run at full speed (134 CFM) at an operating voltage of 12V. The cooling fan on the side of the prototype is also rated at 12V. Still, it is modulated by a digital PWM signal generated in LabVIEW 2020 Software and interfaced by a USB-6112 National Instruments DAQ Card. The gate-to-source voltage is modulated from 0 to 5 V by digitally changing the PWM signal's duty ratio at 1Hz. A single MOSFET controls each fan. The drain to source potential voltage is fixed at 12V.

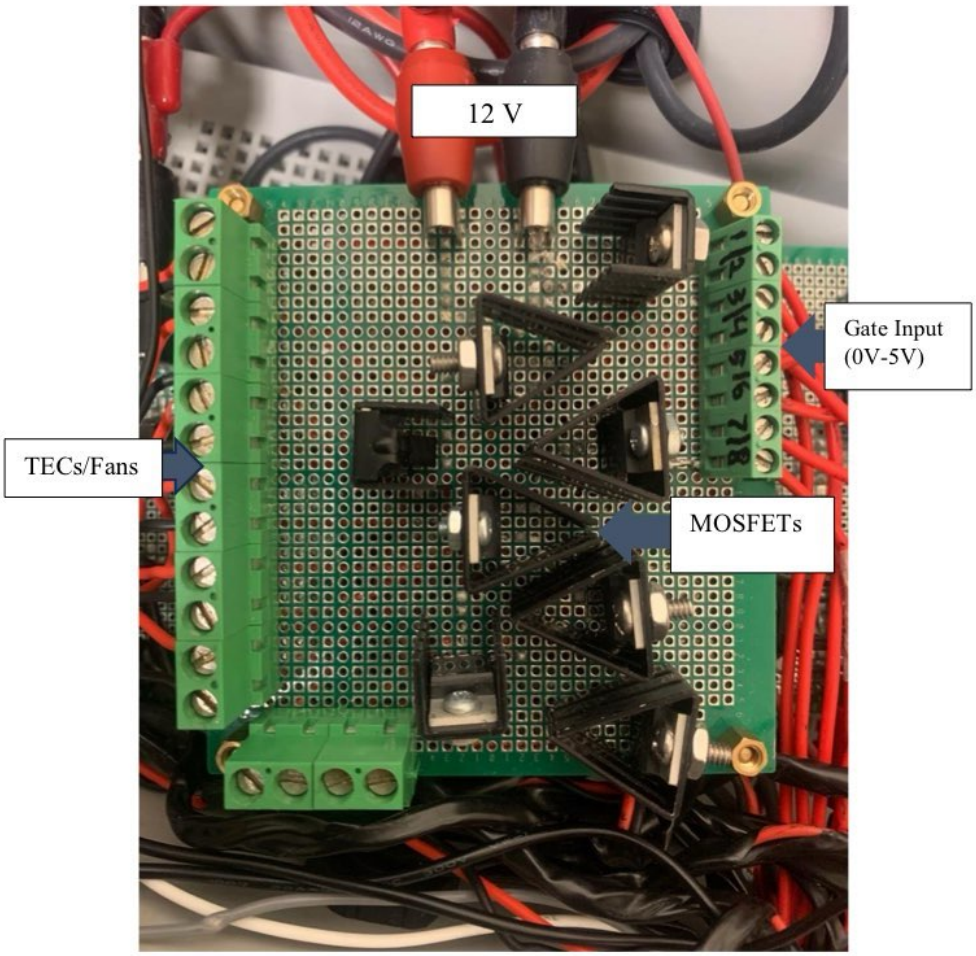

Figure 2.14: Thermoelectric and Fan-driving PCB circuit.

4.1.3 Temperature Sensing Circuit

A total of seven k-type thermocouples are placed along the prototype. Three thermocouples are on the hot side, three on the cooling channel, and one on the outside of the prototype to register ambient temperature. Each thermocouple is driven by a precision thermocouple amplifier with a cold compensator, as shown in Fig. 2.15 and 2.16. Each thermocouple is K-Type, and it is capable of registering temperatures from $-270℃$ to $1372℃$. However, the thermocouple amplifier with cold compensators must be kept at a temperature range of 0℃ to 50℃ to operate effectively. The maximum input voltage of the thermocouple amplifiers is 5V. Therefore, a 12V to 5V voltage regulator is placed in the circuit, as shown in Figure 2.17. The thermocouples were calibrated by comparing the sensors with a mercury thermometer at various temperature changes from 10℃ to 70℃ to minimize the offset.

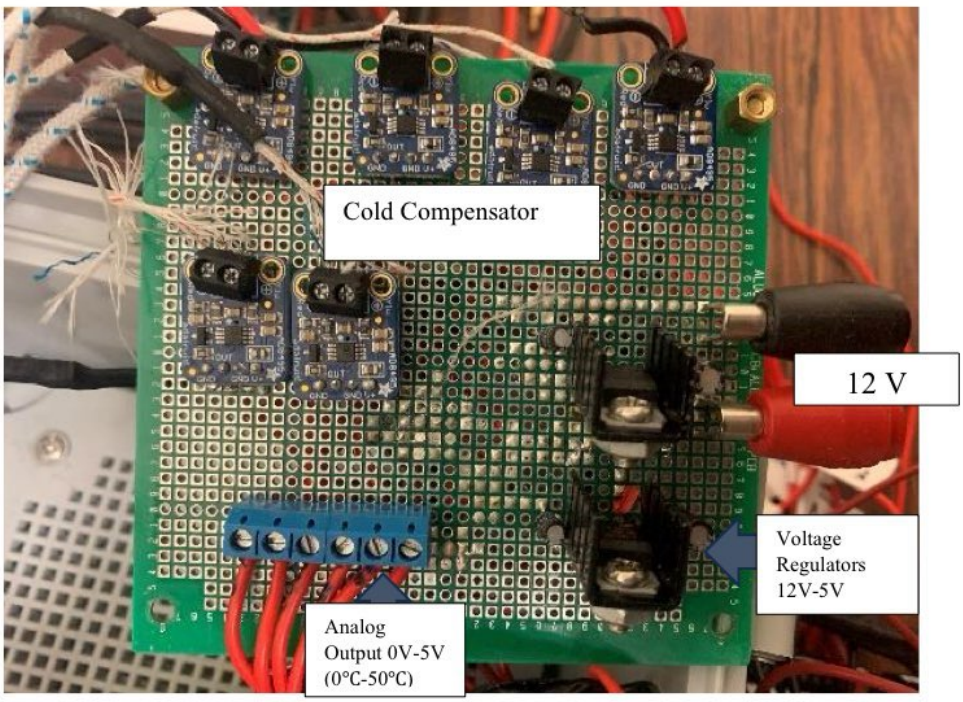

Figure 2.15: Precision thermocouple amplifier with cold compensator PCB circuit

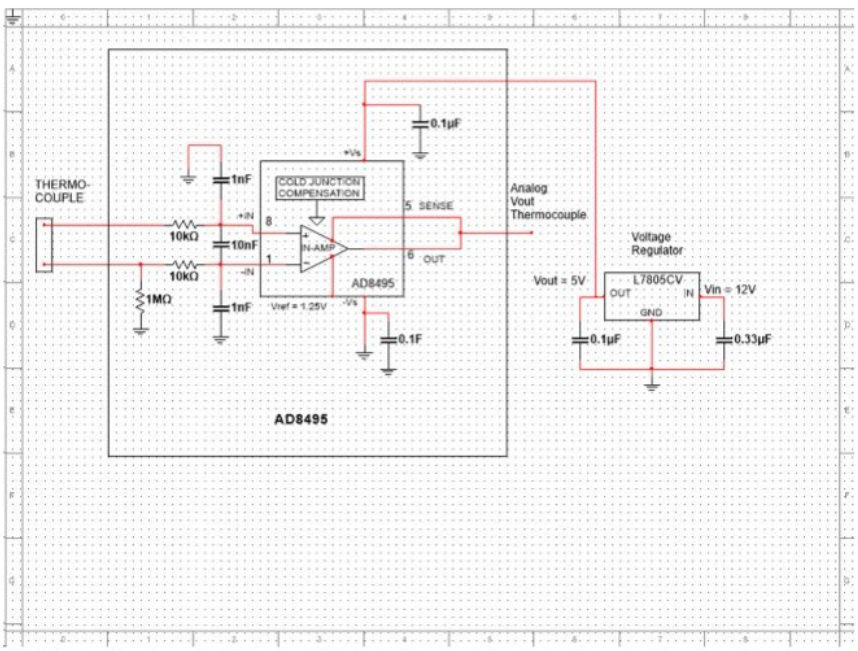

Figure 2.16: PCB Temperature sensing Circuit amplifier with cold compensator

4.1.4 Humidity Sensing Circuit

A total of three humidity sensors are placed along each module. One is on the inlet cooling channel, another is on the outlet cooling channel, and another is far from the module to register room humidity. The analog humidity sensor is shown in Figure 2.17. The humidity sensor circuit schematic is shown in Figure 2.18, and the PCB design in Figure 2.19. The humidity sensors were calibrated by comparing the sensors with an industrial, highly accurate humidity sensor (by Omega Inc) at various humidity conditions from 20% relative humidity to 70% and minimizing the offset.

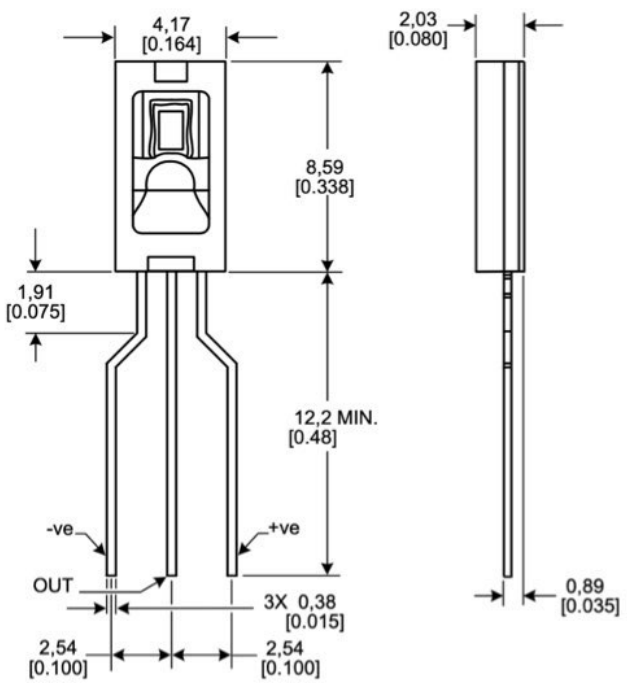

Figure 2.17: Honeywell Analog Humidity Sensor (HIH-4000) Schematic

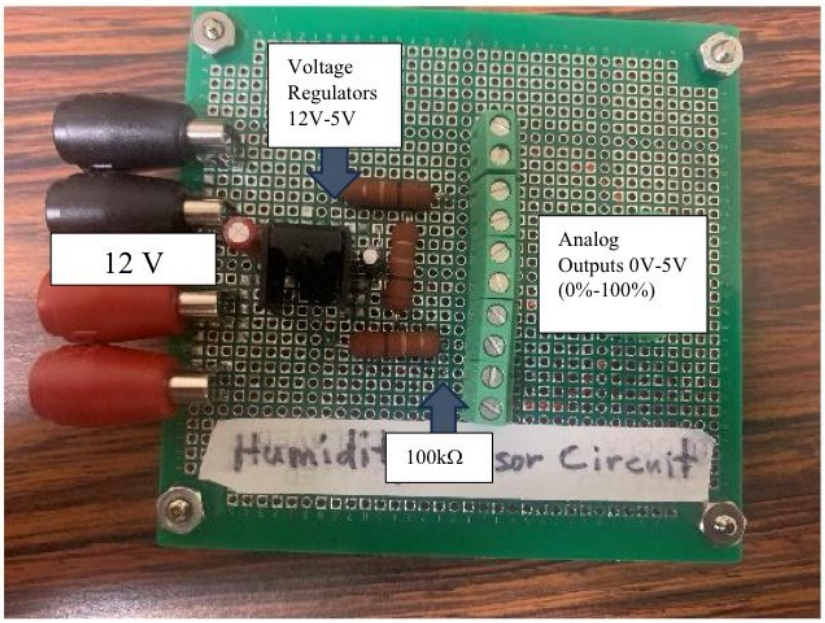

Figure 2.18: Humidity Driving PCB Circuit

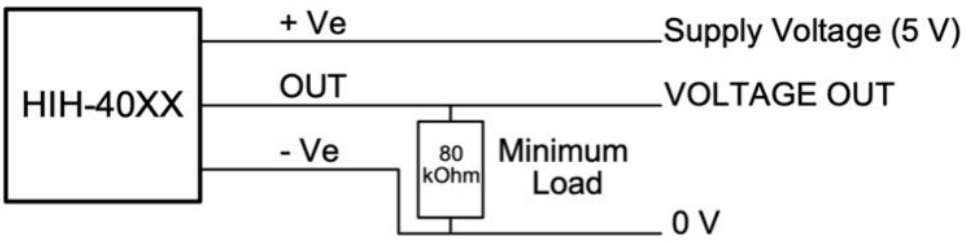

Figure 2.19: Humidity Driving Schematic

4.2 Programming Overview

The AWH thermoelectric cooling modules and fans are controlled and regulated by a simulated pulse width modulation signal (PWM) with a magnitude of 0 to 5 volts and a frequency of 1Hz. The PWM signal is digitally generated using LabVIEW 2020 Software, and the signal is interfaced with the AWM prototype using a USB-6112 National Instruments DAQ card. The DAQ card outputs the signal into the gate MOSFETs of the TECs and fans. By digitally modulating the PWM signal's duty ratio, the gate of the MOSFET controls the average current provided to all six thermoelectric coolers and the fans. The program displays the temperature of each thermocouple (in total, six) by picking up the analog output voltages through the DAQ car. Then, inside LabVIEW, the voltages are transformed to temperatures (in degrees Celsius) and displayed in the front panel. The same principle is applied to the humidity sensors.

4.2.1 TEC Control Software

The first LabVIEW program is shown in Figure 2.20; it drives the TECs by providing 5V to the gate of the MOSFET transistors whenever the set temperature is less than the measured temperature. When the set temperature is greater than or equal to the measured temperature, the program outputs 0V at the gate of the MOSFET. This continuous change of gate voltage closes and opens the MOSFETs, allowing and stopping the current flow of the TECs. This turns the TECs on and off according to the permitted temperature threshold. The front panel of the program plots the raw dynamic temperatures of the cold side, and it takes their average and plots them in a different graph that compares the average measured

temperature and the set temperature. Indicators display the program conditions in the low left corner of the front panel.

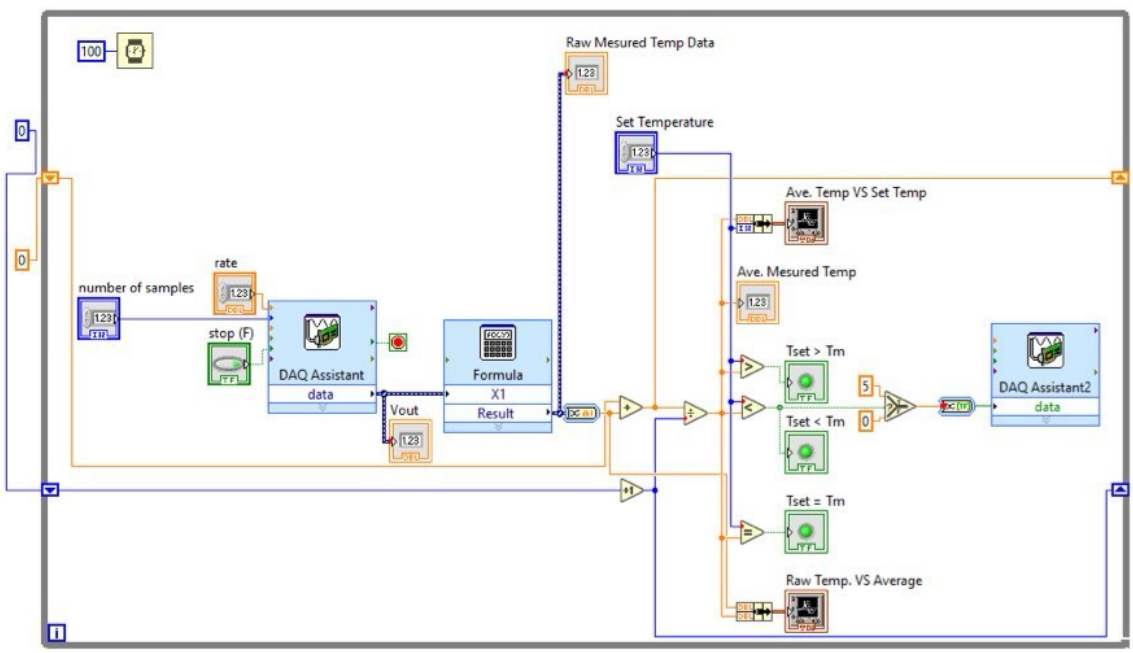

Figure 2.20: Comparator LabVIEW program for TECs.

4.2.2 Fan Control Software

The fan is under your control, and a pulse and a modulation signal are generated in the program. It is a square sinusoidal signal with a frequency of 1Hz and a peak-to-peak voltage of 0 to 5. Figure 2.21 shows the block diagram of the program. The signal is generated and parametrized in LabVIEW and then sent to the gate of the MOSFETs. By varying the percentage of duty cycles, the average current across the fans can be controlled to pre-set parameters.

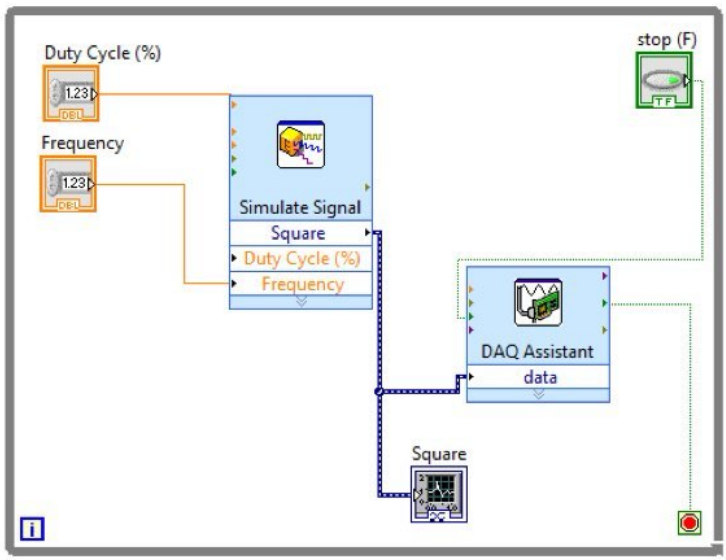

Figure 2.21: PWM Signal LabVIEW program for TECs.

4.2.3 LabVIEW Data Acquisition of the Temperature

The temperature circuit uses precision thermocouple amplifiers with cold junction compensation. It reads the small change in current from a K-type thermocouple, which is proportional to a change in temperature. The software reads the current output from the amplifier and easily converts the current to temperature in degrees Celsius. Each amplifier is rated at 5V input voltage and reads the output of a single thermocouple. The LabVIEW block diagram is shown in Figure 2.22, and the front panel is shown in Figure 2.23.

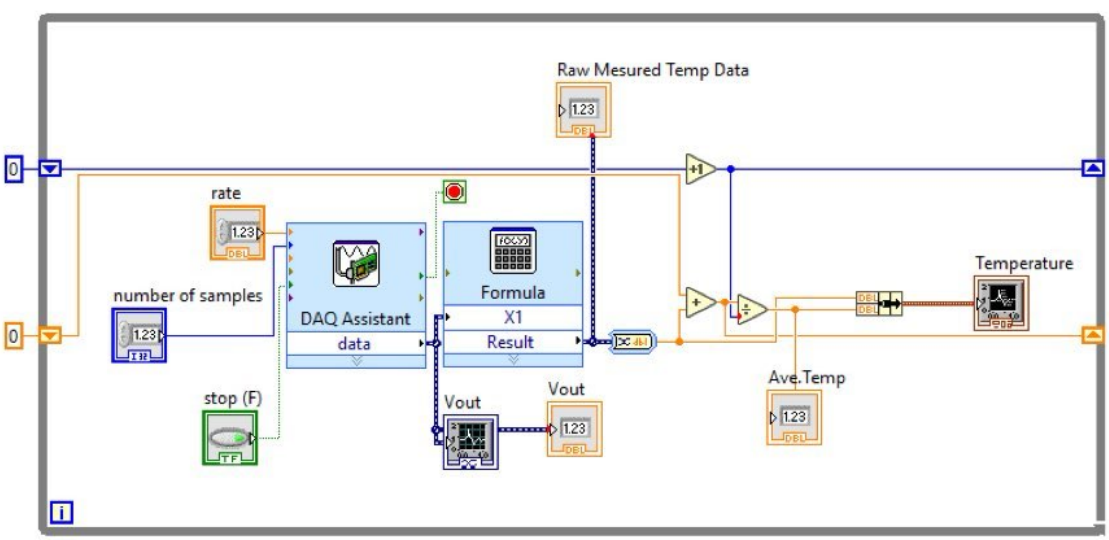

Figure 2.22: LabVIEW block diagram of the temperature sensing program

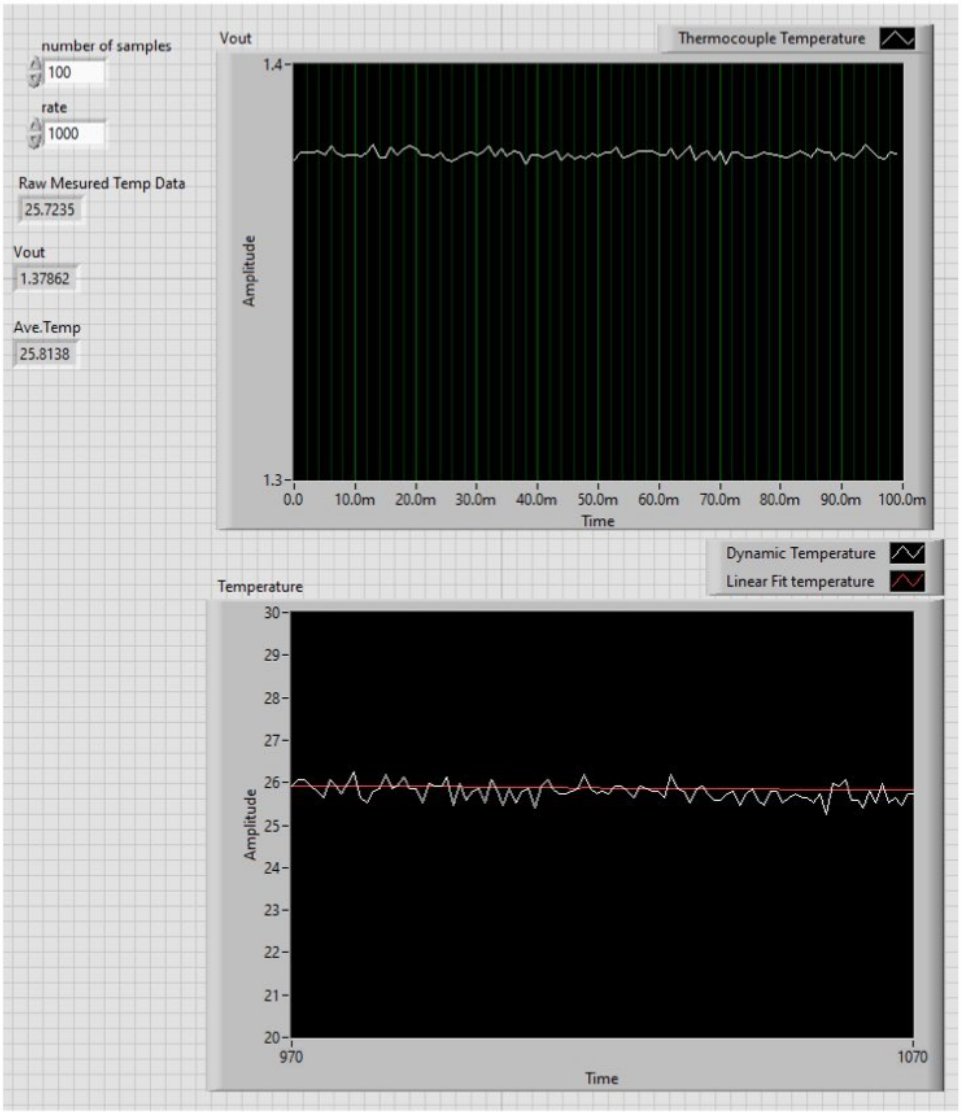

Figure 2.23: LabVIEW front panel of the temperature sensing program

4.2.4 LabVIEW Data Acquisition of the Humidity

The LabVIEW humidity sensor program begins with the DAQ card reading the output voltages of the three analog humidity sensors (HIH-4000-003) at a fixed (previously calculated) sampling rate. Then, it interprets each data point from voltage to humidity using a formula shown in Equation 40. Since the formula is for the sensor calibrated at 25℃ room temperature to get the absolute humidity. Equation 41 was used. To get the room temperature, we use the OMEGA HX303AV humidity sensor. It is highly accurate and reliable. The OMEGA HX303AV sends a variable analog voltage to the DAQ card, and LabVIEW converts the output voltage to temperature using Equation 42. The temperature picked up by the OMEGA sensor is used in Equation 43 to calibrate the HIH-4000-003 humidity sensors at an absolute room temperature and get an accurate actual humidity result. The OMEGA sensor also contains a humidity sensor used as a reference point for the HIH-4000-003 to be calibrated. The OMEGA sensor sends a variable analog output voltage to the DAQ card, and then LabVIEW converts that voltage to relative humidity using Equation 43. Since there was an offset between the HIH-4000-003 sensors and the OMEGA HX303AV sensor, Equation 44 was implemented to get the absolute humidity of all three sensors HIH-4000-003 (assuming the OMEGA HX303AV displays the correct moisture).

$$\mathrm{RH}(\%) = \frac{V_{out} - 0.826}{0.0315} \tag{40}$$

$$\text{True RH}(\%) = \frac{\text{sensor RH}}{1.0546 - 0.00216\mathrm{T}(℃)} \tag{41}$$

$$\mathrm{T}(℃) = V_{out}(100) \tag{42}$$

$$\mathrm{RH}(\%) = \mathrm{V_{out}}(100) \tag{43}$$

$$\text{True RH}(\%) = \frac{\text{sensor RH}}{1.0546 - 0.00216\mathrm{T}(^{\circ}\mathrm{C})} + \text{offset from the OMEGA sensor}(\mathrm{V}) \tag{44}$$

The LabVIEW block diagram shown in Figure 2.24 converts the input analog voltages from the humidity sensors to relative humidity using the procedure discussed in the last paragraph. It simultaneously saves the data into an Excel spreadsheet and plots it on the front panel, as shown in Figure 2.25.

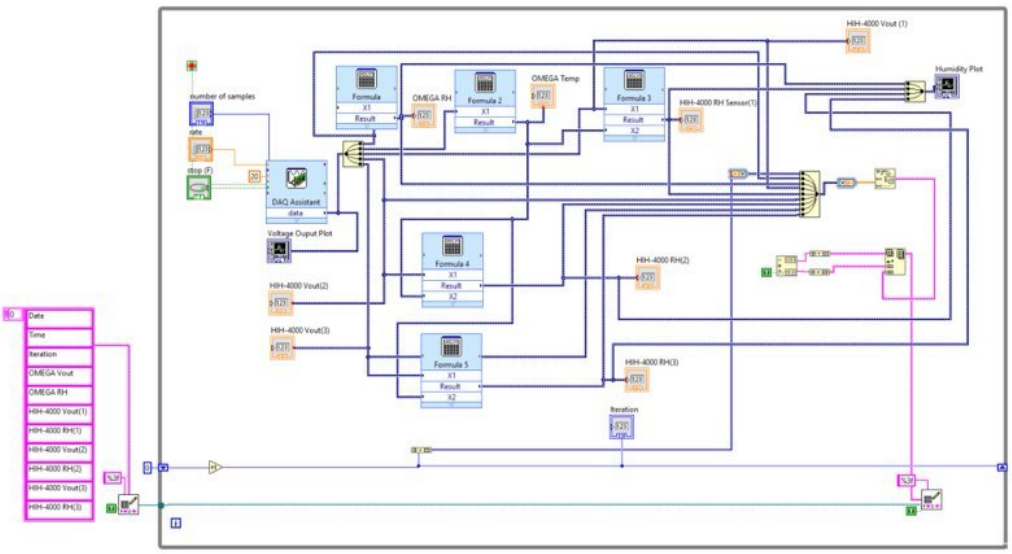

Figure 2.24: LabVIEW Block Diagram

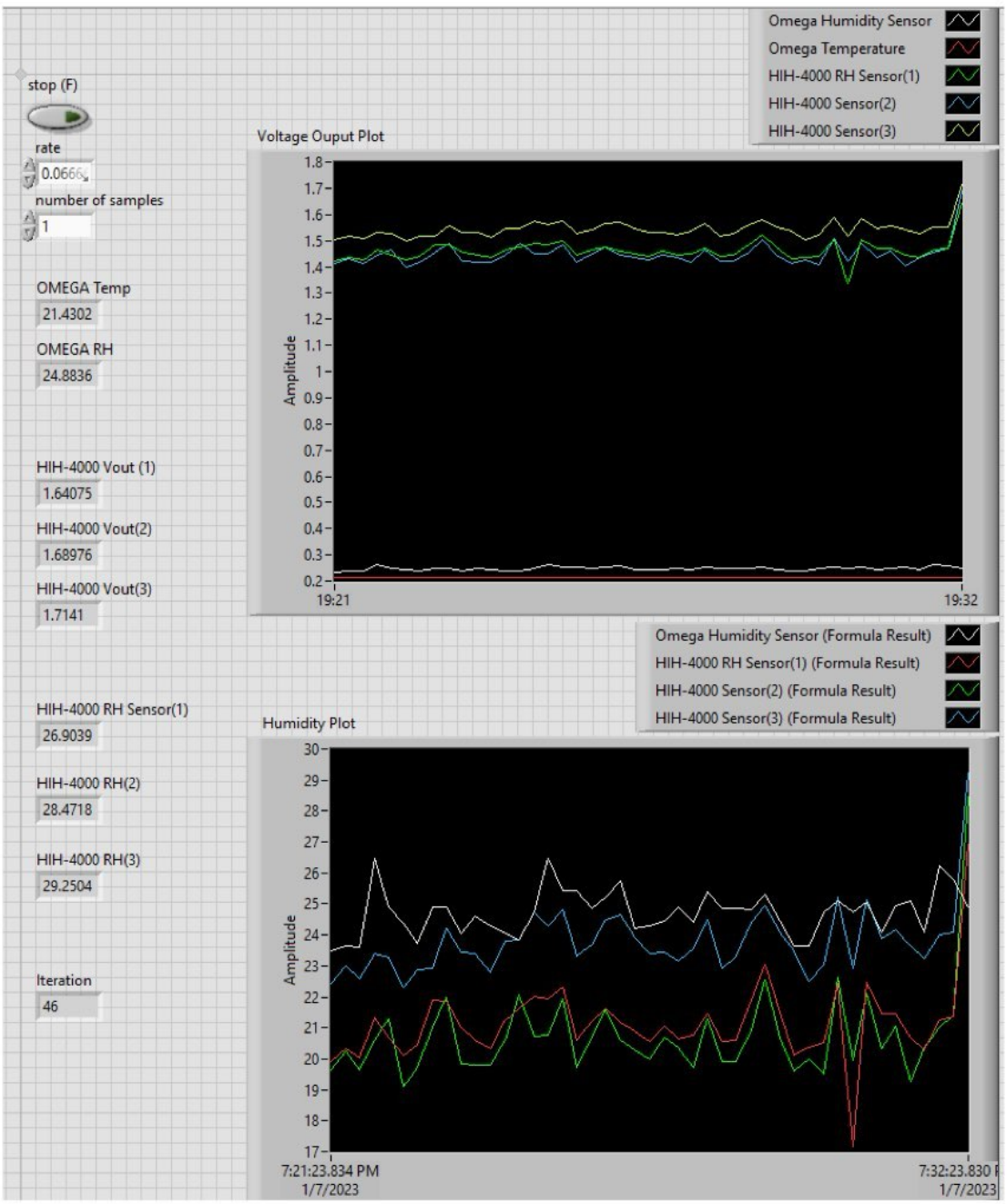

Figure 2.25: LabVIEW Front Panel

4.3 Single Module Mechanical Design Overview

The AWH comprises three separate dehumidifier thermoelectric cooling modules, each composed of one heatsink, two thermoelectric Peltier devices, two cold sinks, and one cooling fan. Figure 2.26 shows the schematic of each dehumidifying cooling module. Each heatsink is black anodized and mounted to the prototype by three mounting holes on each side. The dimensions are 139.7mm long, 38.1mm tall, and 127mm wide. Each sink has 11 fins with a thickness of 3mm and a separation of 5mm. Attached perpendicular to the heatsink is a DC 12V fan supplied by *San Ace* with a rated maximum airflow of 134CFM. The fan is carefully selected to dissipate the heat of the heatsink. Each fan has dimensions of 127mm in length and 127mm in height by 38mm in width. Next, attached to the base of the heatsinks are two evenly spaced thermoelectric Peltier coolers. Each TEC has a maximum temperature difference of 40℃ at a fixed potential of 12V and a current of 4.5A. Therefore, the cooling capacity of each TEC is approximately 20W. Then, attached to each TEC on the cooling side are reflective silver aluminum cool sinks with dimensions of 50mm by 50 mm in length and width. However, the height is 45mm and 40mm for the fins. Each cold sink has six fins in total, and each fin has a thickness of 3mm and a separation of 8mm.

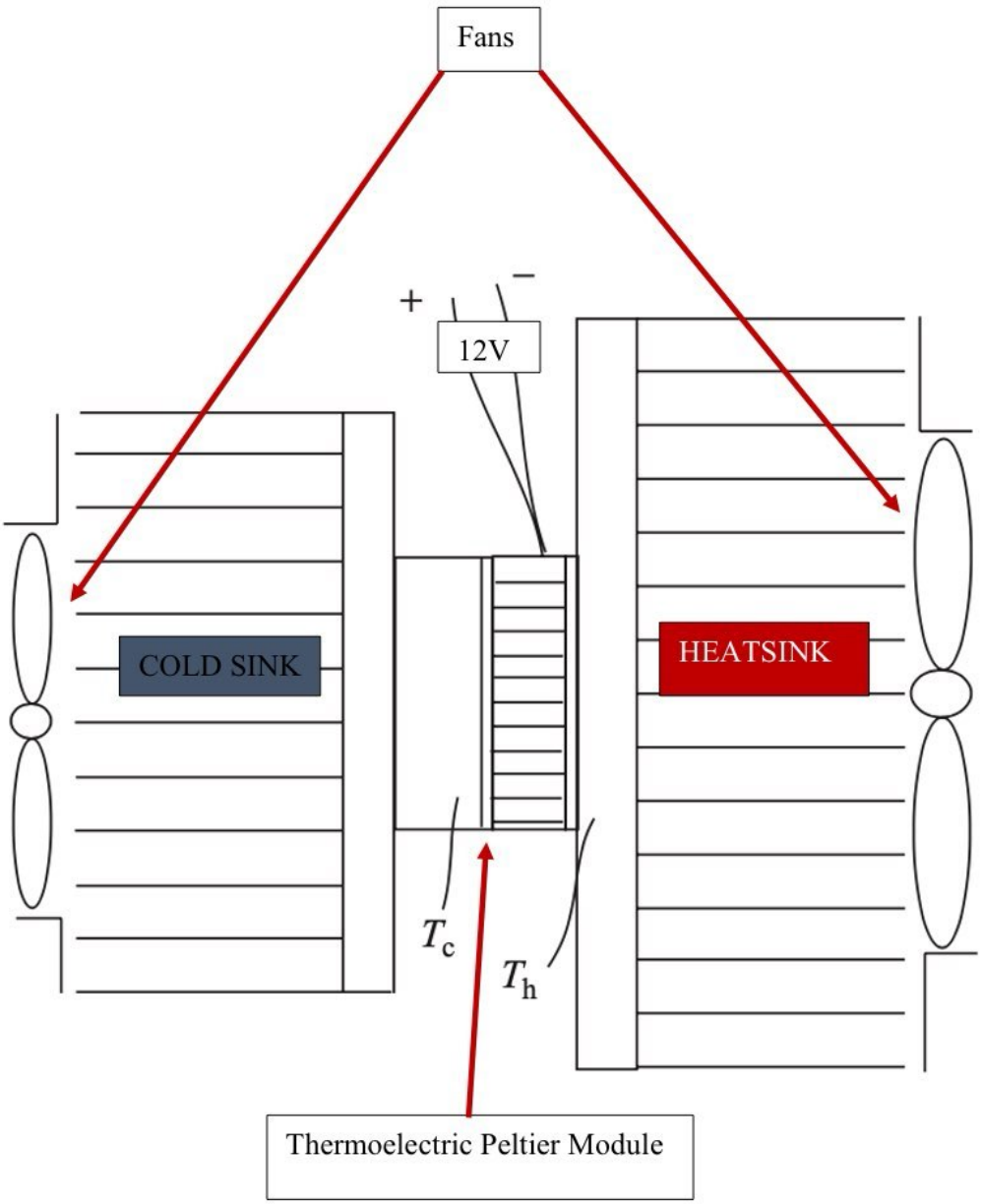

Figure 2.26: Thermoelectric Peltier Module Design Concept

4.3.1 Thermoelectric Peltier Module Selection

Choosing a thermoelectric cooler was difficult, as numerous options are available today. However, the research was parametrized based on the modeling results. Table 2.4 compares prospecting modules that fall within the range of what is adequate for the system by the modeling. They are all proper candidates for the AWM. The thermoelectric cooler selected was the TEC1-12706, shown in Figure 2.27. The selection is based on power consumption and temperature difference.

Next, in the design process, one crucial aspect was using heatsinks. They are an essential component in thermoelectric coolers as they help to dissipate the heat generated by the Peltier device. Heatsinks with rectangular fins and aluminum material are great candidates for the AWH based on the modeling. Heat must be dissipated by force convention airflow. A proposed module was determined based on the chosen heatsink and thermoelectric cooler. Since surface area plays a crucial role in condensation and is inversely proportional to the cold side temperature, several cold sinks were considered.

Table 2.4: TEC1-127 Market Comparison

TYPE	COUPLES	Imax	Umax	Qcmax(w)	ΔTmax (°C)	DIMENSIONS			R	Cost
		(A)	(V)	ΔT =0	Qc=0	(mm)			(Ω)	($)
				Th=27°C		L	W	H		
TEC1-12703	127	3	15.4	26.7	70	40	40	4.9	3.42	14.49
TEC1-12704		4		36.8	70	40	40	4.5	3.02	5.99
TEC1-12705		5		46.5	70	40	40	4.2	2.51	14.99
TEC1-12706		6		53.3	70	40	40	3.8	1.98	9.79
TEC1-12707		7		62.2	70	40	40	3.6	1.71	9.49
TEC1-12708		8		71.1	70	40	40	3.4	1.51	12.99
TEC1-12709		9		80.1	69	40	40	3.4	1.36	13.49
TEC1-12710		10		88.9	69	40	40	3.3	1.08	13.99

Figure 2.27: Thermoelectric Peltier Cooling Device (Model TEC-12706)

4.3.2 Fan

Attaching a fan to the heatsink is crucial for specific reasons, such as increasing airflow and significantly improving heat dissipation. As the air moves over the heartsink's fins, it carries away heat more efficiently. This process is crucial for preventing the hot side of the TEC from overheating since TECs rely on a temperature gradient to function efficiently. If the hot side of the TEC becomes too hot, it diminishes the temperature differential between the hot and cold sides, reducing the cooler's cooling capacity. The fan helps maintain a suitable temperature on the hot side, ensuring that the TEC operates optimally. The fan allows the TEC to operate efficiently by expelling heat more efficiently. This improves cooling performance and reduces energy consumption, as the TEC doesn't need to work as hard to maintain the desired temperature gradient. However, on the hot side, the higher the airflow, the more heat can be dissipated from the heatsink until it reaches a minimum hot temperature settling spot where the fan's speed no longer decreases the hot temperature. This is proportional to the mechanical and thermal properties of the heatsink. Therefore, the cooling fan is chosen under the heatsink parameters, as shown in Figures 2.28 and 2.29. On the other hand, on the cold side, when airflow is introduced to a cold surface, the temperature of the surface can increase due to convective heat transfer. As air flows over the cold side of the TEC, it introduces heat from the surrounding ambient temperature, causing an increase in temperature proportional to the fan's speed. However, since condensation requires a continuous mass transfer rate between the cold surface and the water vapor molecules, it is essential to maintain airflow in the cooling channel. Therefore, an adequate small fan is chosen, as shown in Figures 2.30 and 2.31, in compliance with the

fact that there is a small boundary airflow range that will yield condensation in the cooling channel and the cold sink mechanical and thermal parameters.

Figure 2.28: Dissipating fan attached to the Cooling channel

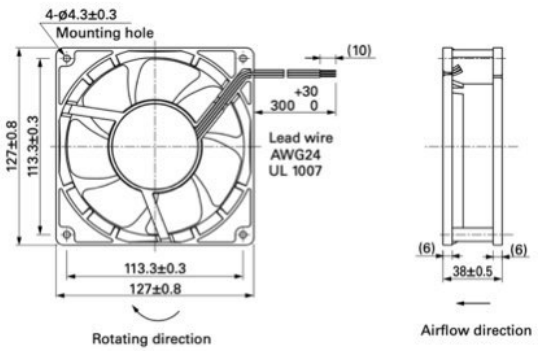

Figure 1.30: Schematic of the dissipating fan attached to the cooling channel

Figure 2.29: Cooling Fan Attached to the heatsink

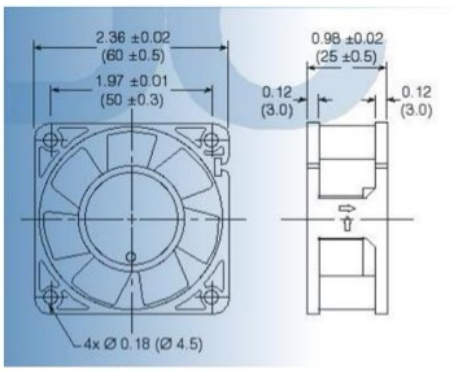

Figure 2.31: Schematic of the cooling fan attached to the heatsink.

4.3.3 Heatsink

Without an effective heatsink, the device's efficiency dramatically reduces and potentially causes damage because any heatsink can dissipate heat efficiently. The heatsink must be big enough to dissipate the heat being dumped from the cold side and the internal heat of each TEC. As the number of TECs per heatsink increases, so does the average hot temperature. The following heatsink, shown in Figures 2.32 to 2.34, is carefully selected to dissipate heat away from the hot side of TECs efficiently. The surface area of the heatsink is carefully chosen in proportion to the required heat transfer, and it is enhanced by forced convectional airflow to carry the heat away. The heatsink is selected in proportion to the theoretical modeling results.

Figure 2.32: Heatsink

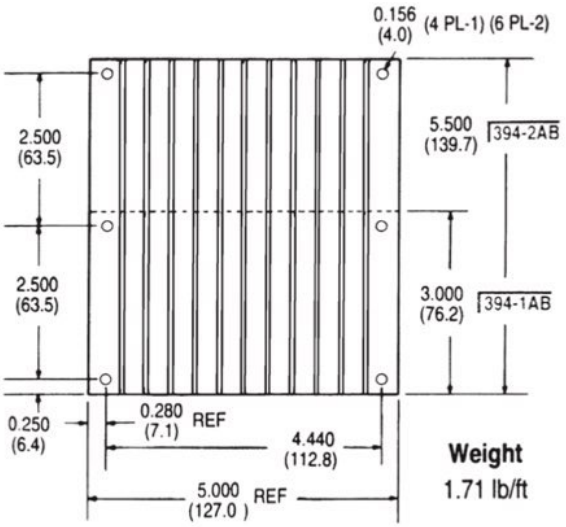

Figure 2.33: Top View Heatsink Schematic

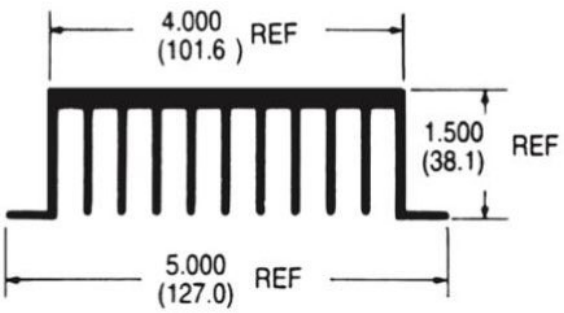

Figure 2.34: Front View Heatsink Schematic

4.3.4 Cold sink

The primary role of a cold sink is to enhance condensation by increasing the space available for water vapor molecules in the air to meet a surface and condense into liquid water droplets. As the surface area increases, it provides more contact points for water vapor molecules to interact with the surface. This increases the likelihood of water vapor molecules encountering the surface and condensing into liquid water droplets. However, one crucial thing to consider carefully is thermal conductivity. If the surface temperature is kept below the dew point, the surface temperature must drop below the dew point of the surrounding air for condensation to occur. Therefore, only specific cold sinks with adequate thermal conductivity can be utilized, particularly aluminum types. The dimensions and number of fins also play an essential role in reaching desirable cooling temperatures. Since the cold sinks are exposed to ambient temperature, heat influx from the environment increases the total average temperature of the cold sinks as the surface area increases drastically. In addition, depending on the cooling capacity of the thermoelectric Peltier cooler it must work harder to remove this additional heat, which decreases total module efficiency and effectiveness in maintaining low temperatures. Though a careful investigation was performed using the chosen heatsink and thermoelectric Peltier modules described above, three cold sink candidates were selected. Therefore, through optimal experimentation and comparison among the three candidates, one was chosen as the adequate candidate for the AWH prototype.

a)

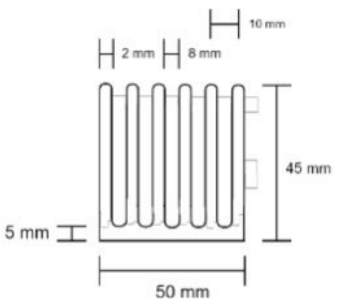

b)

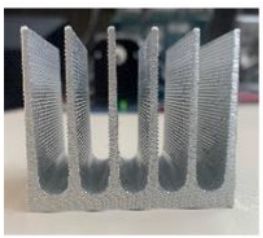

Figure 2.35: Module A a) Front View Schematic, b) Front View Image

a)

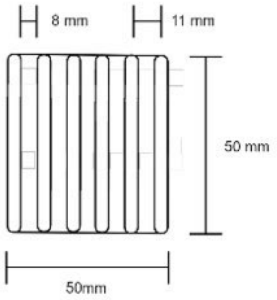

b)

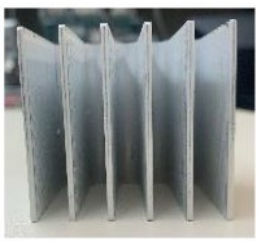

Figure 2.36: Module A a) Top View Schematic, b) Top View Image

a)

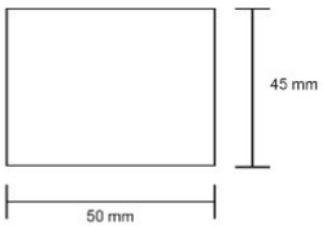

b)

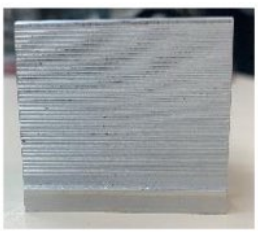

Figure 2.37: Module A a) Side View Schematic, b) Side View Image

First, as shown in Figures 2.35 to 2.37, cold sink A has the tallest fins compared to the rest. They are evenly spaced, and the space between them is the largest compared to cold sinks B and C. The cold sink is made from aluminum alloy.

a)

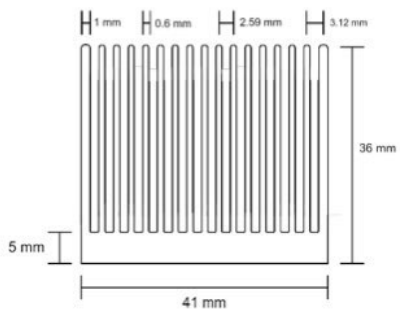

b)

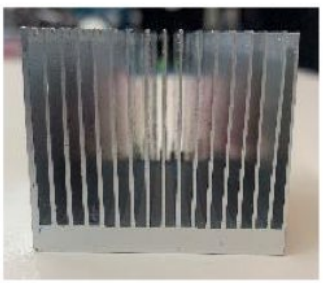

Figure 2.38: Module B a) Front View Schematic, b) Front View Image

a)

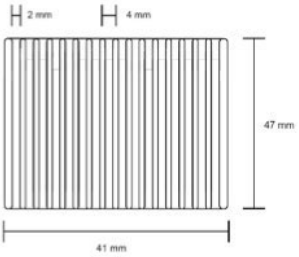

b)

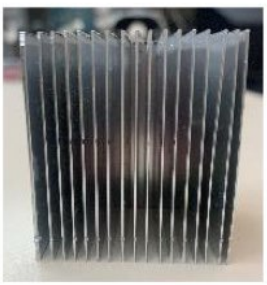

Figure 2.39 Module B a) Top View Schematic, b) Top View Image

a)

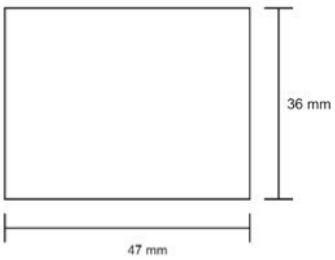

b)

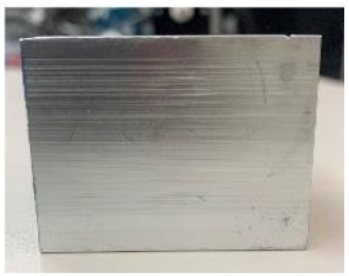

Figure 2.40: Module B a) Side View Schematic, b) Side View Schematic

Next, as shown in Figures 2.38 to 2.40, cold sink B has the most fins compared to the rest. They are evenly spaced, and the space between them is smallest compared to cold sinks A and C. The cold sink is made from aluminum alloy. Cold sink B has the largest exposed surface area.

a)

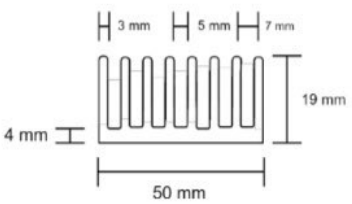

b)

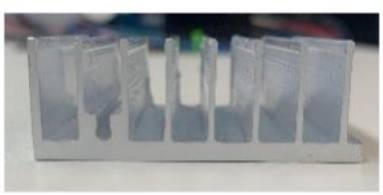

Figure 2.41: Module C a) Front View Schematic, b) Front View Image

a)

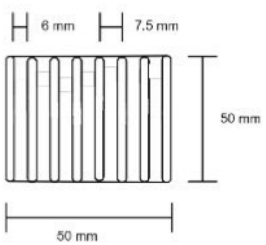

b)

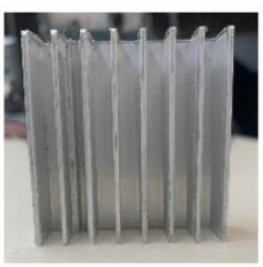

Figure 2.42: Module C a) Top View Schematic, b) Top View Image

a)

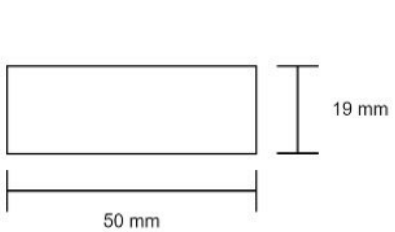

b)

Figure 2.43: Module C a) Side View Schematic, b) Side View Image

Then, as shown in Figures 2.41 to 2.43, cold sink C has the shortest fins compared to the rest. They are evenly spaced, and the space between them is more significant than between cold sink B and smaller than between cold sink A. The cold sink is made from aluminum alloy.

4.3.5 Single Module Design

Utilizing the cold sinks, the heatsink, the fans, and the TECs described in the preview sections, Modules A, B, and C were designed as shown in Figures 2.44 to 2.46. Each module is composed of two TECs. Each module operates at a fixed 12V potential. One thermocouple is placed inside the sinks, and two humidity sensors are placed on the cold side per Module. The cooling fan attached to the heatsink has a downward airflow direction perpendicular to the top surface of the heatsink. The dissipating fan attached to the cold side has an airflow parallel to the top surface of the cold sink. The modules are shown in Figures 2.47 to 2.49. Each module is compared and characterized in the following section.

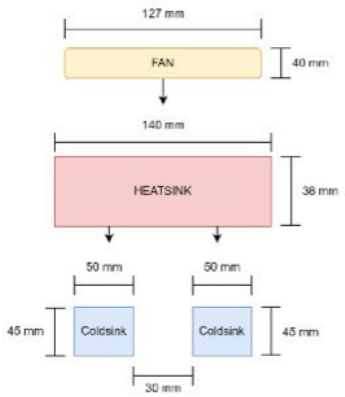

Figure 2.44: Schematic of Module A.

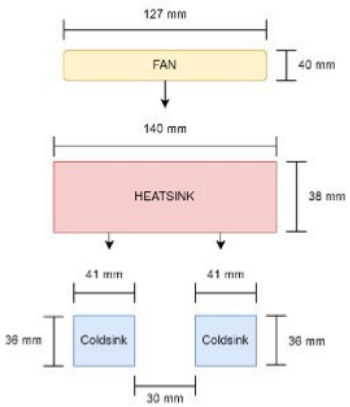

Figure 2.45: Schematic of Module B.

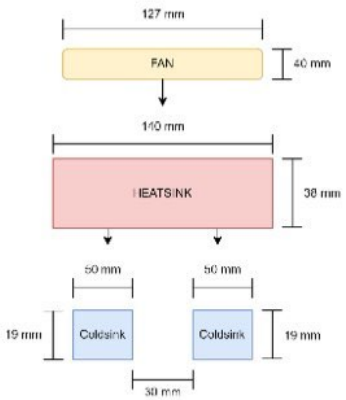

Figure 2.46: Schematic of Module C.

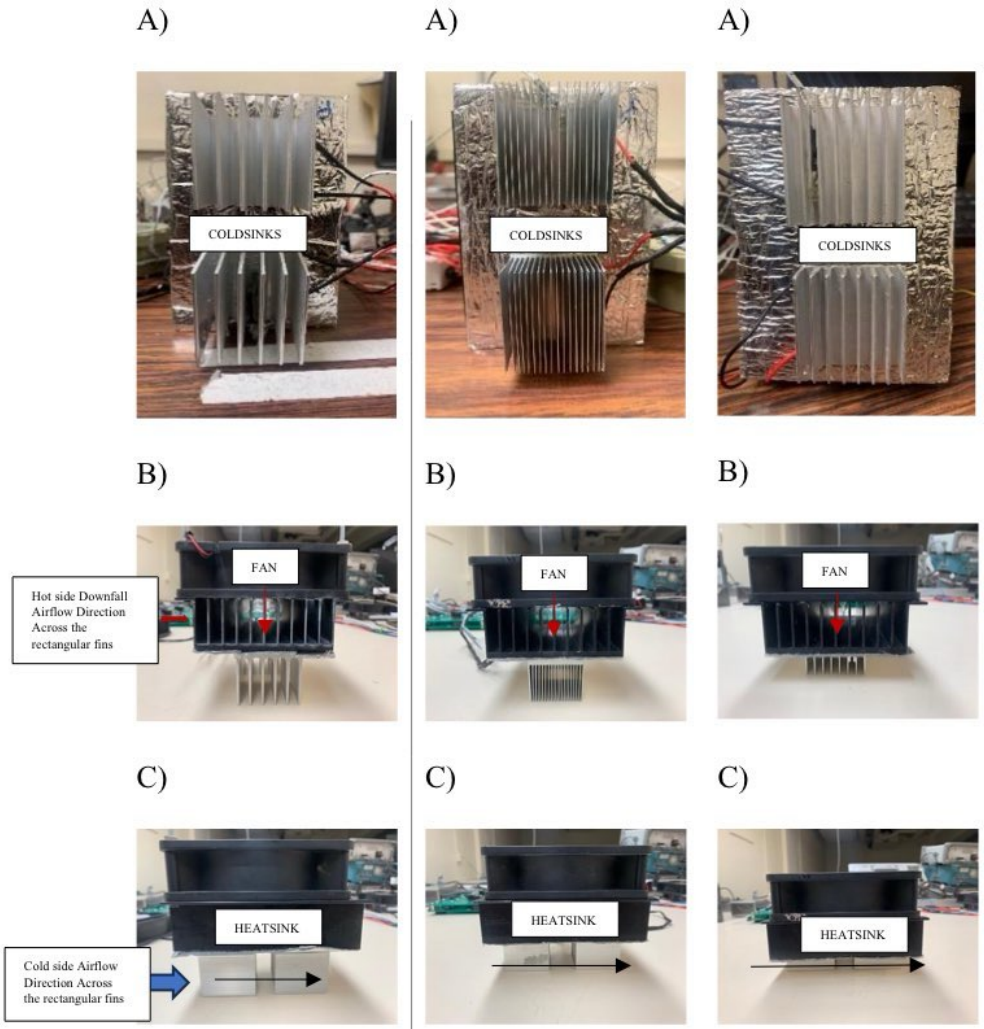

Figure 2.47: Module A A) Top Image. B) Front Image. C) Side Image.

Figure 2.48: Module B A) Top Image. B) Front Image. C) Side Image.

Figure 2.49: Module C A) Top Image. B) Front Image. C) Side Image.

5. Single Module Comparison and Optimization

The first step in module characterization was power consumption. Each module had maximum fan-capable airflow input across the fins on the hot side but zero airflow on the cold side. The power was varied every hour, and it was done so by inputting a PWM 1Htz frequency signal to highly controllable switching MOSFETs driving the TECs. Each point was replicated three times in one hour, and the experiments were performed at lab parameters. From Figures 2.50 to 2.52, it can be concluded that a maximum duty ratio of 100% yields the most significant temperature difference between the hot and cold sides and the optimal spot for input power per module. This is directly proportional to the allowed operating temperature range for each module. The greater the temperature range, the higher the efficiency of the module. Module B yields the highest temperature difference between the hot and cold side (42.5°C) at a 100% duty ratio, and Module A the lowest (39.2°C).

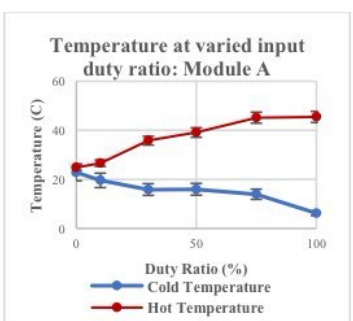

Figure 2.50: Temperature distribution of the module at varied input PWM (1Hz) duty ratio signal at 20% relative humidity, 25°C ambient temperature, 134CFM airflow on the hot side, and zero airflow on the cold side.

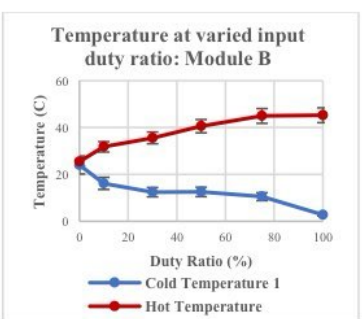

Figure 2.51: Temperature distribution of the at varied input PWM (1Hz) duty ratio signal at 20% relative humidity, 25°C ambient temperature, 134CFM airflow on the hot side, and zero airflow on the cold side.

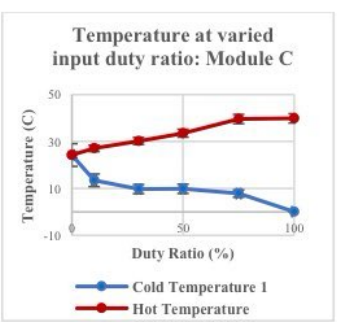

Figure 2.52: Temperature distribution of the module at varied input PWM (1Hz) duty ratio signal at 20% relative humidity, 25°C ambient temperature, 134CFM airflow on the hot side, and zero airflow on the cold side.

Subsequent experiments were performed at an ambient temperature of 25°C and relative humidity of 20% to assess changes in cold temperature as airflow is varied. The hot side cooling airflow was kept at 135 CFM (the optimal point), and each experiment was run for one hour and replicated three times at every airflow point, as shown in Figures 2.5**3** to 2.5**5**. The input power of the TECs is maintained and constantly measured at an optimal power input. The input airflow on the cooling channel was measured and varied by implementing the same Pulse Width Modulation programming setup implemented above. However, the PWM frequency varied by the desired measured output airflow of the fan shown in Figures 2.5**3** to 2.5**5**. From the resulting data, it can be concluded that an airflow higher than 12.56 CFM for all modules significantly affected the average temperature of the cooling channel. However, anything lower than 12.56 CFM did not significantly change the temperature. Therefore, the optimal airflow speed of the fan must be within the range of 0.1 to 12.56 CFM.

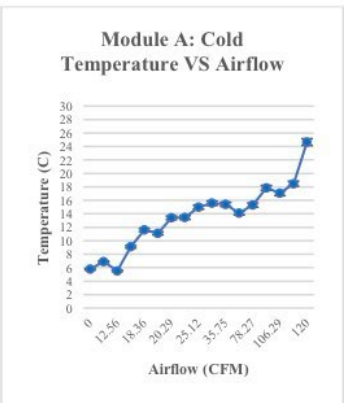

Figure 2.53: Average cold sink temperature as a function of forcing convection airflow across the fins.

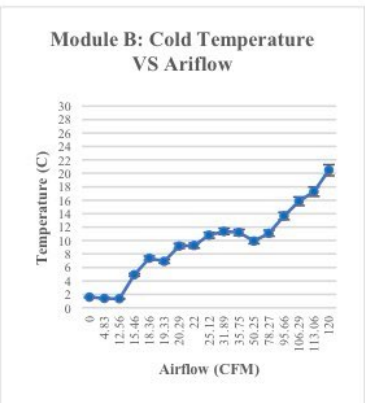

Figure 2.54: Base cold sink temperature as a function of force convection airflow across the fins.

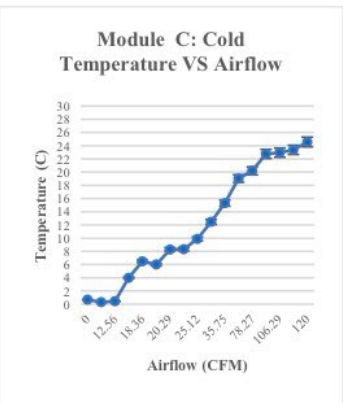

Figure 2.55: Base cold sink temperature as a function of force convection airflow across the fins.

Next, each module was independently tested for water collection at various airflow speeds and relative humidity points, ignoring the average temperature in the cooling channel. The ambient temperature was kept at 25℃ and the cooling fan attached to the heatsink was kept and constantly measured at 135 CFM. Figures 2.56 to 2.58 show that Module A yields the highest water condensation rate. 12.75 ml/h at 22 CFM input airflow and RH of 70%. The humidity was controlled by enclosing each module in a designed environmental chamber with a manually set humidifier wrapped with thermal isolation foam. Module A produced more water at all RH points than the other modules. The results are influenced by fin spacing and airflow through the heatsink. Narrower fin spacing creates more resistance to airflow, which can reduce the flow rate of air passing through the heatsink. This, in turn, causes the water droplets to remain adhered to the cold sink's surface, preventing new droplet formations. Module B has the highest surface area but the shortest fin gap; it condenses more than the other two modules due to the amount of surface exposed, but the fin spacing traps water droplets in between due to the capillary tension of the fin walls and the airflow cannot overcome such tension. Module A has the second highest surface area but the most significant fin gap; it condenses more than Module C due to the amount of surface exposed, but the fin spacing allows more uniform airflow to reach the water droplets and break capillary tension off the fin walls.

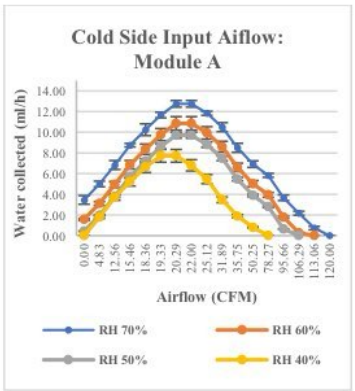

Figure 2.56: Module A amount of water produced (in ml/h) as a function of forced convection airflow across the fins (in CFM) for various humidity points.

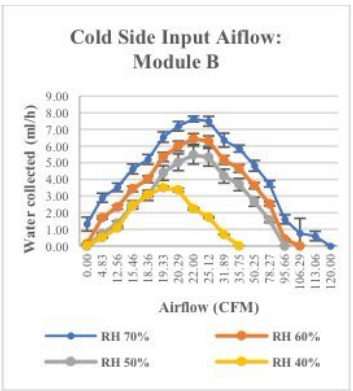

Figure 2.57: Module B amount of water produced (in ml/h) as a function of forced convection airflow across the fins (in CFM) for various humidity points.

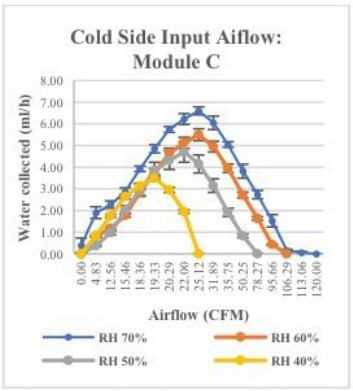

Figure 2.58: Module C amount of water produced (in ml/h) as a function of forced convection airflow across the fins (in CFM) for various humidity points.

Table 2.5: Optimum input cold channel airflow at every RH % point and an ambient temperature of 25°C.

RH %	40%	50%	60%	70%
Module A	19.33 CFM	20.29 CFM	20.29 CFM	20.29 CFM
Module B	19.33 CFM	22.5 CFM	22.5 CFM	22.5 CFM
Module C	19.33 CFM	22.0 CFM	25.12 CFM	25 CFM

According to Table 2.4, the optimum cold side input airflow changes as the humidity increases. Thus, the following experiment was performed at those parameters, including an ambient temperature of 25°C and optimal fan speed on the hot side. The results are shown in Figures 2.59 to 2.61 and the same results in Figures 2.56 to 2.58. The experiment is controlled inside the same environmental characteristics as the previous experiment. However, the airflow in the cooling chamber is at a determined optimum rate per RH variations. Therefore, the following water rates are the maximum capable water collection each Module can offer after optimization of the airflow.

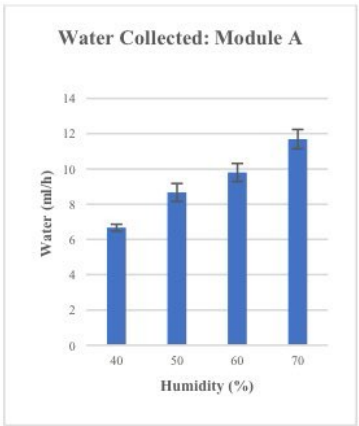

Figure 2.59: Water collected for Module A as a function of changing relative humidity at optimum forced convection airflow

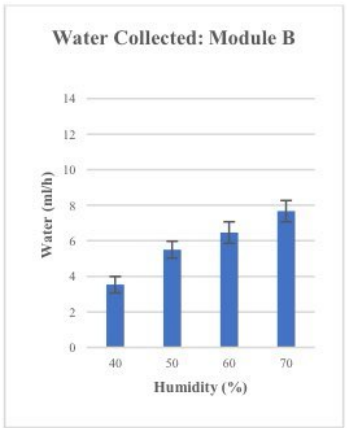

Figure 2.60: Water collected for Module B as a function of changing relative humidity at optimum forced convection airflow.

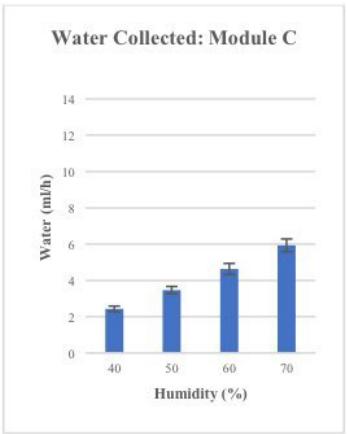

Figure 2.61: Water collected for Module C as a function of changing relative humidity at optimum forced convection airflow.

Figures 2.65 to 2.67 show the output temperature distribution of each module at optimal conditions for one hour at room temperature of 25°C, 70% relative humidity, 54W input power to the TECs per TEC, an average of 134 CFM airflow on the hot side, and 22CFM input airflow on the cooling chamber. Figures 2.62 to 2.64 show samplings of the water collected per Module. Module C has the lowest temperature but the least amount of

condensation. This is because the Module has the smallest surface area exposed to condensation.

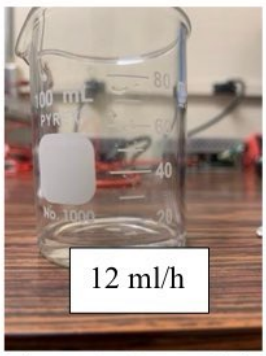

Figure 2.62: Module A Experimental Sampling Water Collected

Figure 2.63: Module B Experimental Sampling Water Collected

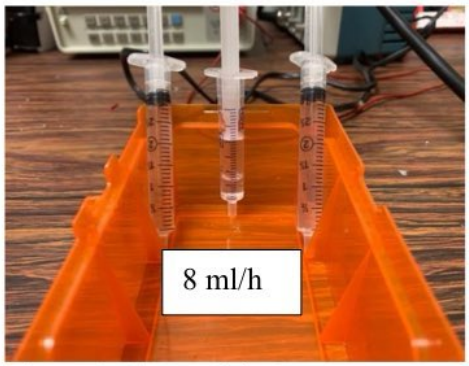

Figure 2.64: Module C Experimental Sampling Water Collected

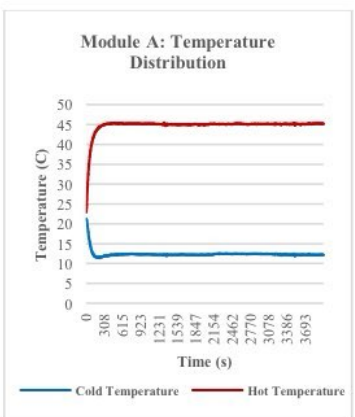

Figure 2.65: Temperature Distribution of Module A at optimized parameters.

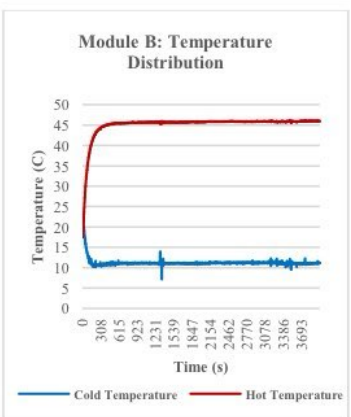

Figure 2.66: Temperature Distribution of Module B at optimized parameters.

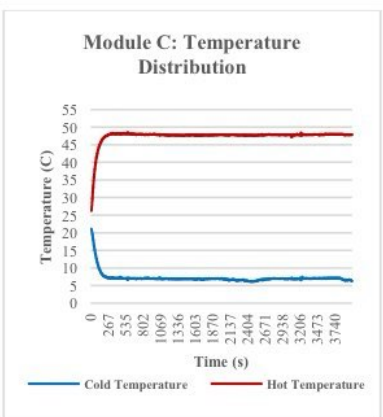

Figure 2.67: Temperature Distribution of Module C at optimized parameters.

Figures 2.68 to 2.72 show the thermophysical parameters of Module A at optimal conditions. The average temperature difference between the hot and cold sides is around 33 degrees. The module's heat dissipation rate is higher than its heat absorption rate. The total power consumption of the module is around 67W, and the COP is 0.3.

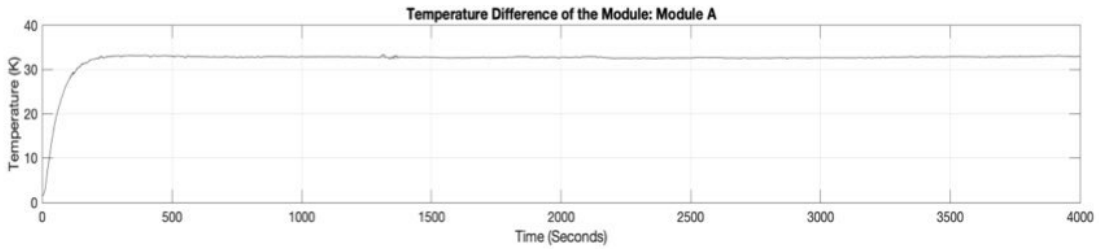

Figure 2.68: Changes in temperature difference between the hot and cold side of Module A, optimum parameters.

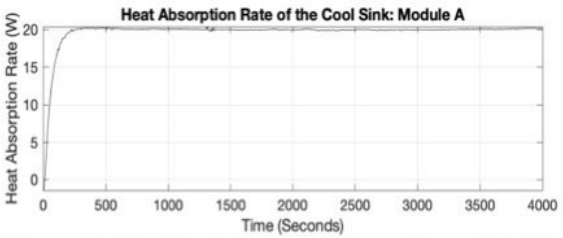

Figure 2.69: Heat removed from the cold side at optimum parameters.

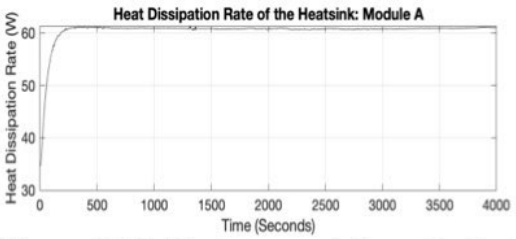

Figure 2.70: Heat removal from the hot side, optimum parameters.

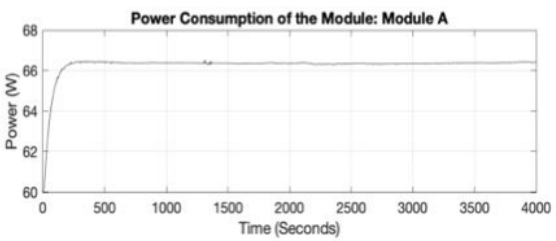

Figure 2.71: Changes in the input power to the TECs as a function of time at optimum parameters.

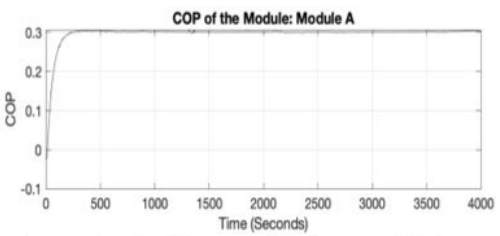

Figure 2.72: Changes in the coefficient of performance as a function of time at optimum parameters.

Figures 2.73 to 2.77 show the thermophysical parameters of Module B at optimum conditions. The average temperature difference between the hot and cold sides is maintained at around 40 K or °C. The module's heat dissipation rate is higher than its heat

absorption rate. The total power consumption of the module is around 67W, and the COP is 0.7.

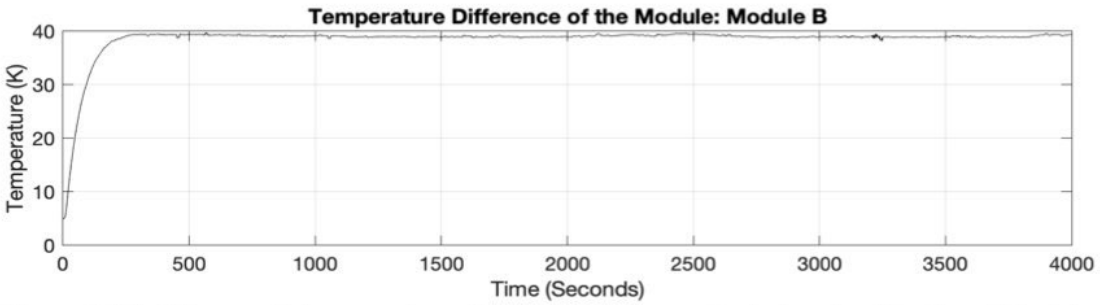

Figure 2.73: Changes in temperature difference between the hot and cold side of Module B at optimum parameters.

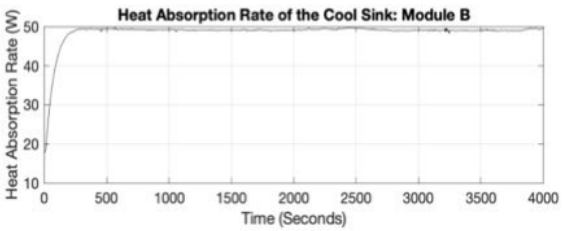

Figure 2.74: Heat removed from the cold side, optimum parameters.

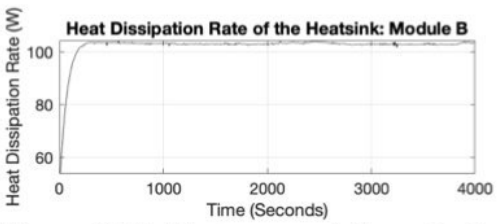

Figure 2.75: Heat removal from the hot side at optimum parameters.

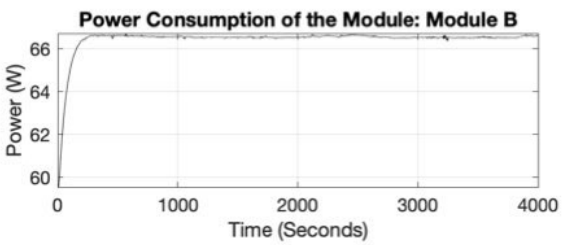

Figure 2.76: Changes in the input power to the TECs as a function of time at optimum parameters.

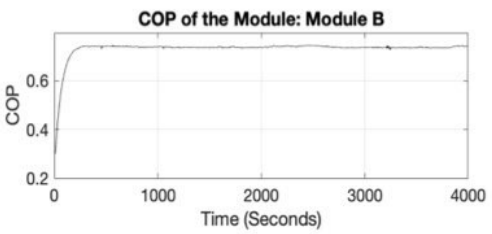

Figure 2.77: Changes in the coefficient of performance as a function of time at optimum parameters.

Figures 2.78 to 2.82 show the thermophysical parameters of Module C at optimum conditions. The average temperature difference between the hot and cold sides is maintained around 33 K or ℃. The heat dissipation rate of the Module is higher than the heat dissipation rate. The total power consumption of the module is around 67W, and the COP is 0.7.

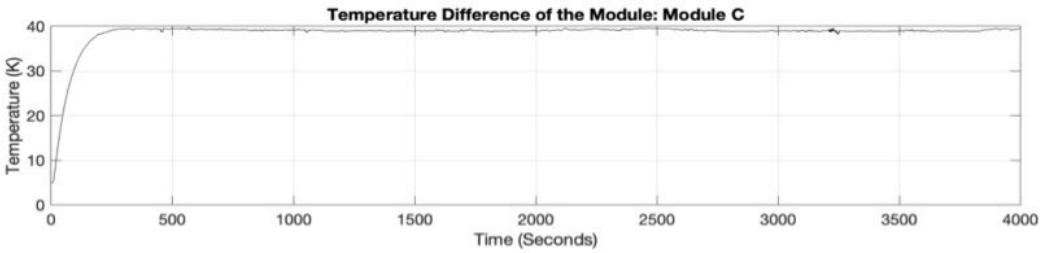

Figure 2.78: Changes in temperature difference between the hot and cold side of Module C at optimum parameters.

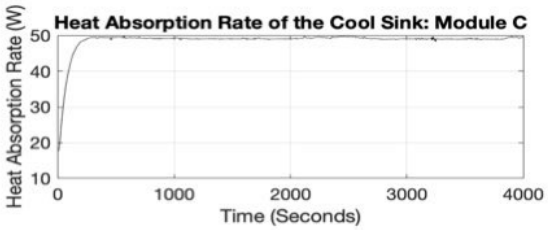

Figure 2.79: Heat removed from the cold side at optimum parameters.

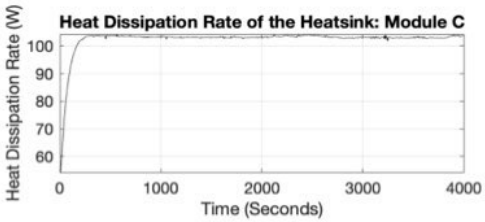

Figure 2.80: Heat removal from the hot side at optimum parameters.

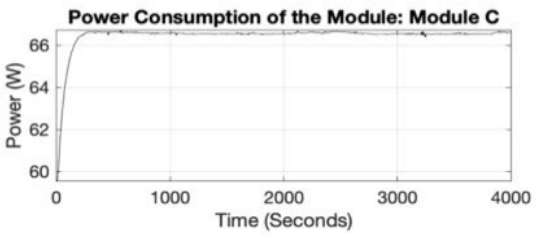

Figure 2.81: Changes in the input power to the TECs as a function of time at optimum parameters.

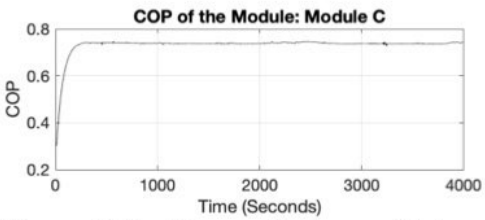

Figure 2.82: Changes in the coefficient of performance as a function of time, at optimum parmeters.

In conclusion, Module A is the most adequate for the atmospheric water harvesting prototype. The module yields the highest rate of water condensation at all humidity points. The structure of the cooling sinks allows for efficient water droplet formation. For example, Module B has the largest surface area but a minimal fin separation, which caused water droplets to get trapped in the cooling sinks and prevented the new formation of droplets on the surface. Optimal conditions for maximum water rate collection at room temperature of 25°C are 70% relative humidity, a maximum input power per TEC, an average of 134 CFM airflow on the hot side, and 22CFM input airflow on the cooling chamber.

References

[1] D. Zhao and G. Tan, "A review of thermoelectric cooling: Materials, modeling, and applications," *Appl. Therm. Eng.*, vol. 66, no. 1, pp. 15–24, May 2014, doi: 10.1016/j.applthermaleng.2014.01.074.

[2] V. Patel, R. Patel, and J. Patel, "Theoretical and experimental investigation of bubble column humidification and thermoelectric cooler dehumidification water desalination system," *Int. J. Energy Res.*, vol. 44, no. 2, pp. 890–901, 2020, doi: 10.1002/er.4931.

[3] M. Eslami, F. Tajeddini, and N. Etaati, "Thermal analysis and optimization of a system for water harvesting from humid air using thermoelectric coolers," *Energy Convers. Manag.*, vol. 174, pp. 417–429, Oct. 2018, doi: 10.1016/j.enconman.2018.08.045.

[4] G. Tang, S. M. Rabeek, and M. A. Arasu, "Thermal design and temperature gradient analysis for a thermoelectric energy harvest device in an off-shore and marine application," in *2016 IEEE 18th Electronics Packaging Technology Conference (EPTC)*, Nov. 2016, pp. 648–652. doi: 10.1109/EPTC.2016.7861560.

[5] K. Almutairi, K. Irshad, S. Algarni, A. Ali, and S. Islam, "Experimental investigation of dehumidification process regulated by the photothermoelectric system," *Water Sci. Technol. J. Int. Assoc. Water Pollut. Res.*, vol. 84, no. 10–11, pp. 3211–3226, Nov. 2021, doi 10.2166/wst.2021.368.

[6] M. Jradi, N. Ghaddar, and K. Ghali, "Experimental and theoretical study of an integrated thermoelectric–photovoltaic system for air dehumidification and fresh water production," *Int. J. Energy Res.*, vol. 36, no. 9, pp. 963–974, 2012, doi: 10.1002/er.1848.

[7] J. G. Vián, D. Astrain, and M. Domínguez, "Numerical modelling and a design of a thermoelectric dehumidifier," *Appl. Therm. Eng.*, vol. 22, no. 4, pp. 407–422, Mar.
2002, doi: 10.1016/S1359-4311(01)00102-8.

CHAPTER 3: ATMOSPHERIC WATER HARVESTING PROTOTYPE

1. Objective

The AWH is composed of two major parts, three thermoelectric cooling modules (designed and characterized in the previews chapter) enclosed in a prototyped hosing, and a thermoelectric cooling and sensor driving circuit.

2. Conceptual Prototype Design Principle

The AWH prototype incorporates six TECs and three thermoelectric cooling modules incorporated in an acrylic housing encasement. Cool, humid air is sucked into the system by an intake fan into a cooling chamber where the air is cooled by the three cold sinks enclosed in an isolated cooling chamber. As temperatures drop below the dew point of the air, condensation begins to happen inside the cooling chamber. Tiny water droplets accumulate in the chamber and are collected in a water container. The prototype is powered and controlled by an autonomous 12V DC power supply (that can be easily charged with solar panels), a control system using a DAQ card as the interface and LabVIEW as the controlling software, and a driving circuit that monitors and runs the sensors and thermoelectric coolers Figure 3.1 and 3.2 shows a schematic and flowchart of the conceptual system design of the prototype.

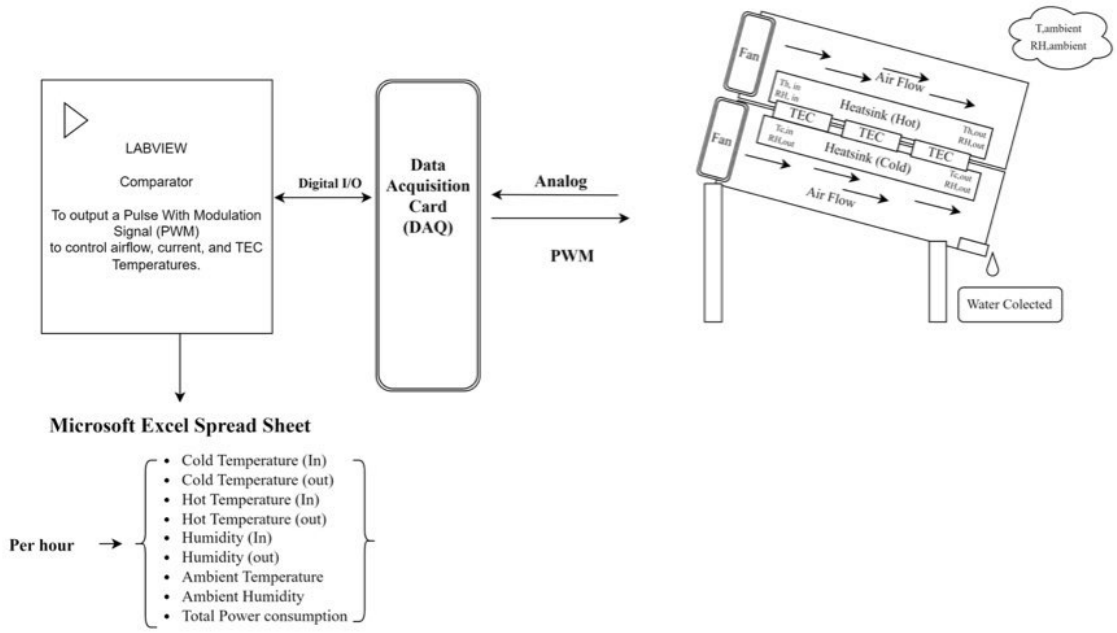

Figure 3.1: Schematic of the conceptual system design principle

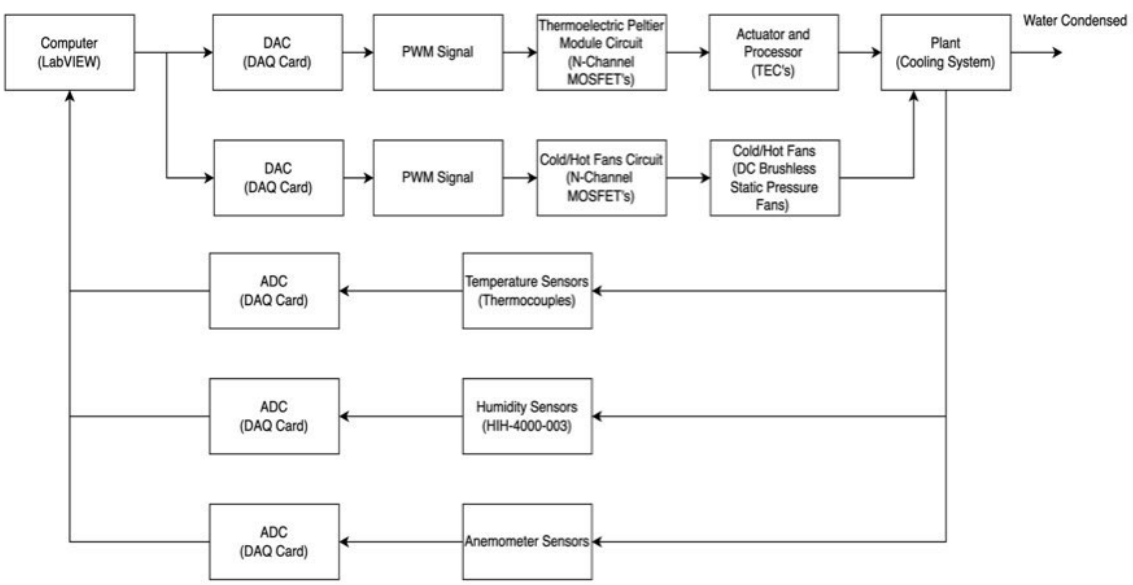

Figure 3.2: Conceptual Flowchart diagram of the system design principle

3. Encasement Design

The Atmospheric Water Harvesting (AWH) encasement was designed using standard engineering and architectural principles. The encasement's primary purpose is first to hold the thermoelectric modules in place at the desired position angle. Second, the hot side of the thermoelectric modules must be isolated entirely from the cold side. Third, the structure of the cooling channel must be well-suited for evenly distributed input airflow, pressure, temperature, and humidity. Fourth, the prototype must have an effective way to collect condensed water, minimizing losses. Lastly, it must be desktop-sized and easy to transport. Therefore, the encasement was designed as shown in Appendix B and by the desired standards and previously designed prototypes in Figures 3.3 to 3.5.

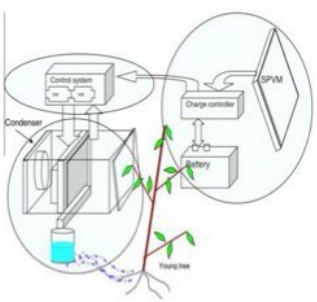

Figure 3.3: Muñoz-García Experimental system prototype [2]

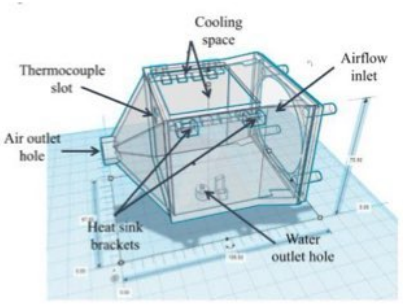

Figure 3.4: Shanshan et al. Schematic prototype [3]

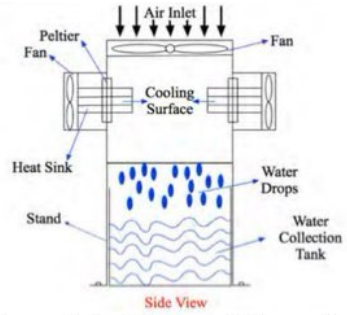

Figure 3.5: Alenezi Schematic of the water harvester prototype [1]

The prototype encasement was built with ½-inch-thick acrylic sheets, each joined using an acrylic welder.

4. AWH Prototype System

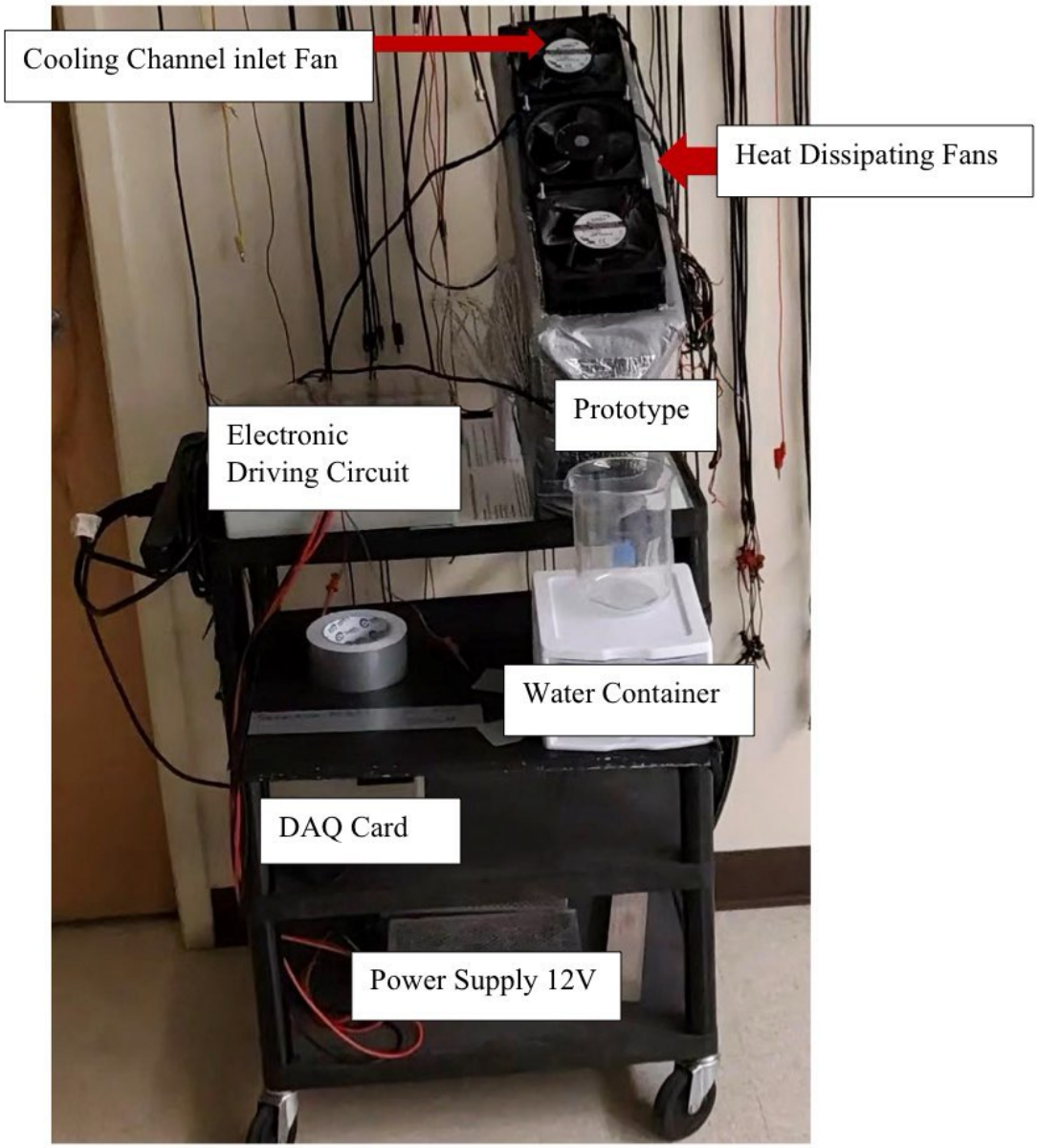

Figure 3.6: AWH Prototype and Experimental System (front view)

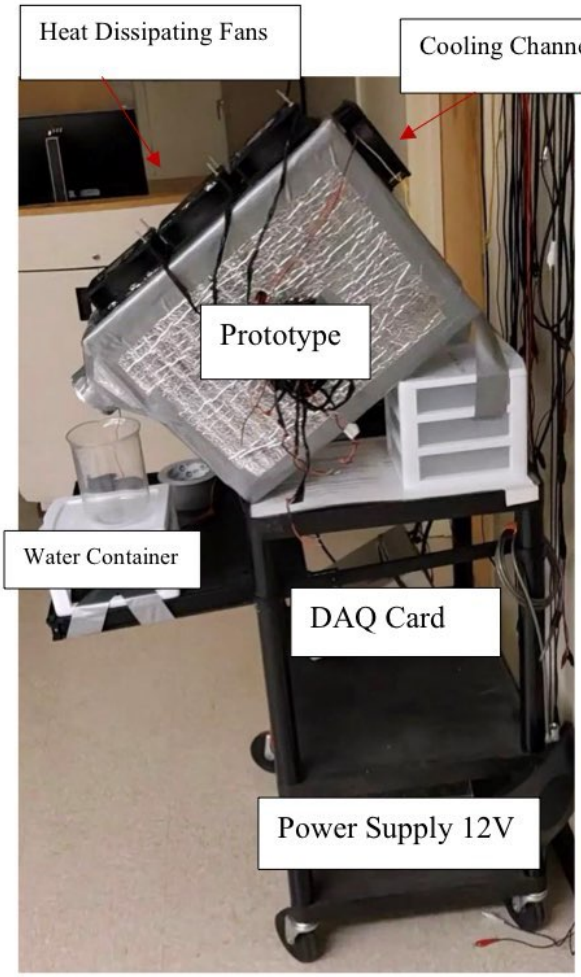

Figure 3.7: AWH Prototype and Experimental System (front view)

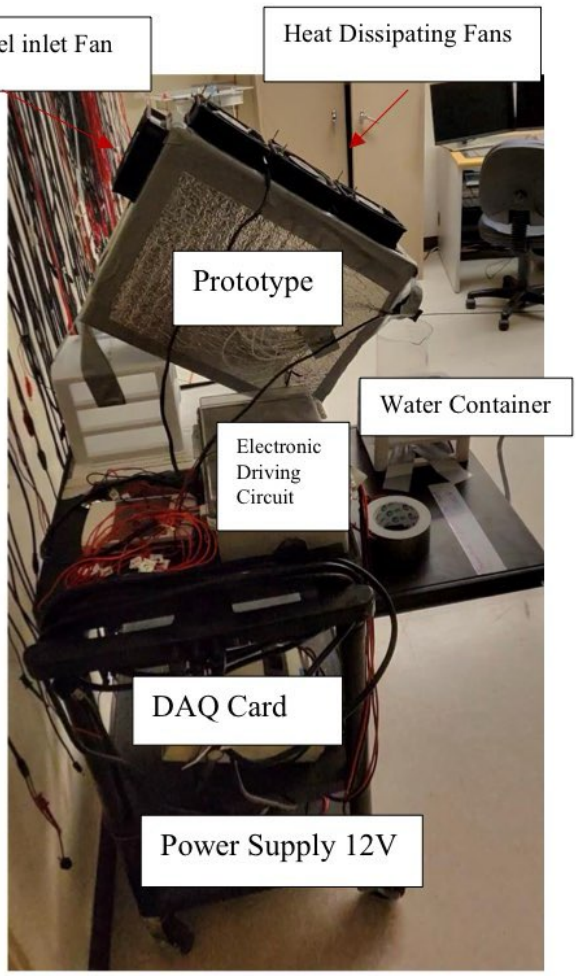

Figure 3.8: AWH Prototype and Experimental System (front view)

5. Prototype Characterizations

Based on the previously identified optimum parameters (in chapter 2). The first step in the prototype characterization was power consumption. The speed of each fan on the hot side was equally set to 135 CFM, but there was zero airflow on the cold side. The power was varied every hour. Figure 3.9 shows that a maximum duty ratio of 100% yields the most significant average temperature difference between the hot and cold sides and the optimal spot for input power per module.

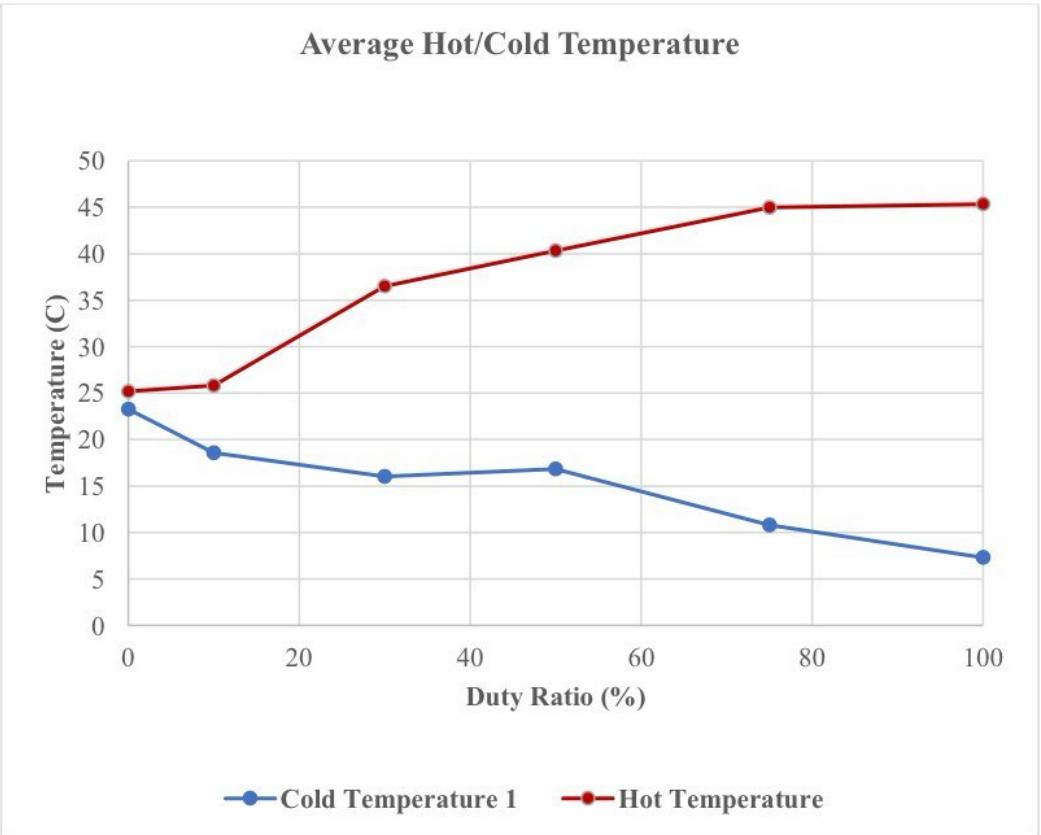

Figure 3.9: Average temperature of the hot and cold sides of the prototype as a function of a varied input PWM (1Hz) duty ratio signal, at 20% relative humidity, 25°C ambient temperature, 134CFM airflow on the hot side and zero airflow on the cold side.

Next, the prototype was tested for optimal input airflow in the cooling channel. The experiment was performed at optimal conditions; it was run for one hour and replicated three times at every airflow point, as shown in Figure 3.10. The input power of the TECs is maintained and constantly measured at an optimal power input. The resulting data shows that an airflow higher than 18.36 CFM affects the cooling channel's average temperature significantly. However, anything lower than 18.36 CFM did not significantly change the temperature. Therefore, the optimal airflow speed of the fan must be within the range of 0 to 18.36 CFM. Module C yields the lowest temperatures at the optimal airflow range.

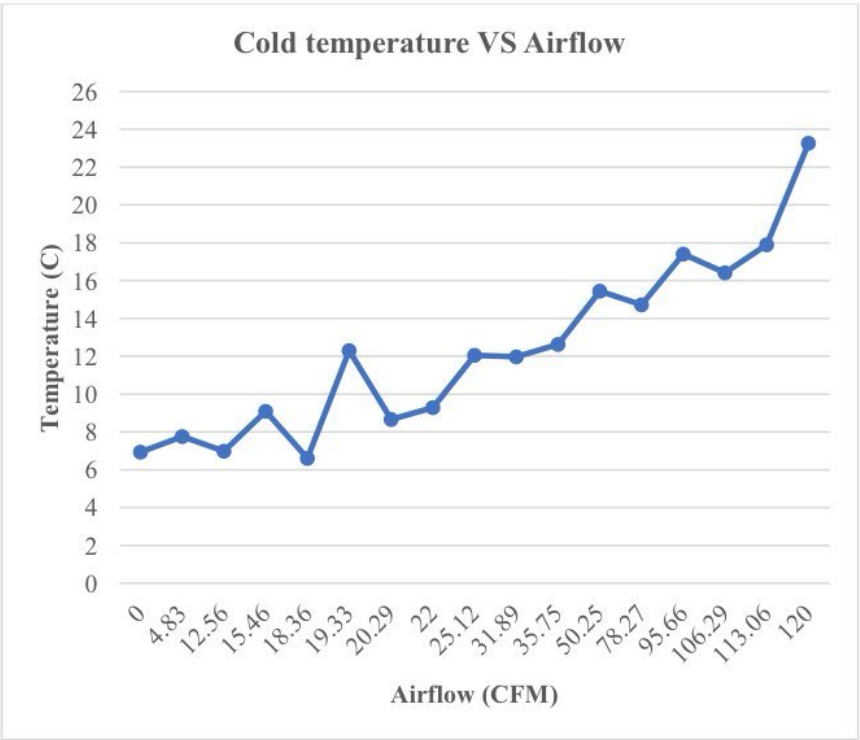

Figure 3.10: Average cold sink temperature as a function of force convection airflow across the fins at 20% relative humidity, 25°C ambient temperature, 134CFM airflow on the hot side, and zero airflow on the cold side.

Next, the prototype was tested for water collection at various airflow speeds and relative humidity points, ignoring the average temperature in the cooling channel. The ambient temperature was kept at 25℃ and the cooling fan attached to the heatsink was kept and constantly measured at 135 CFM. According to Figure 3.11, at 20.29 CFM input airflow and RH of 70%, the prototype yields a maximum water collection rate of 39 ml/h.

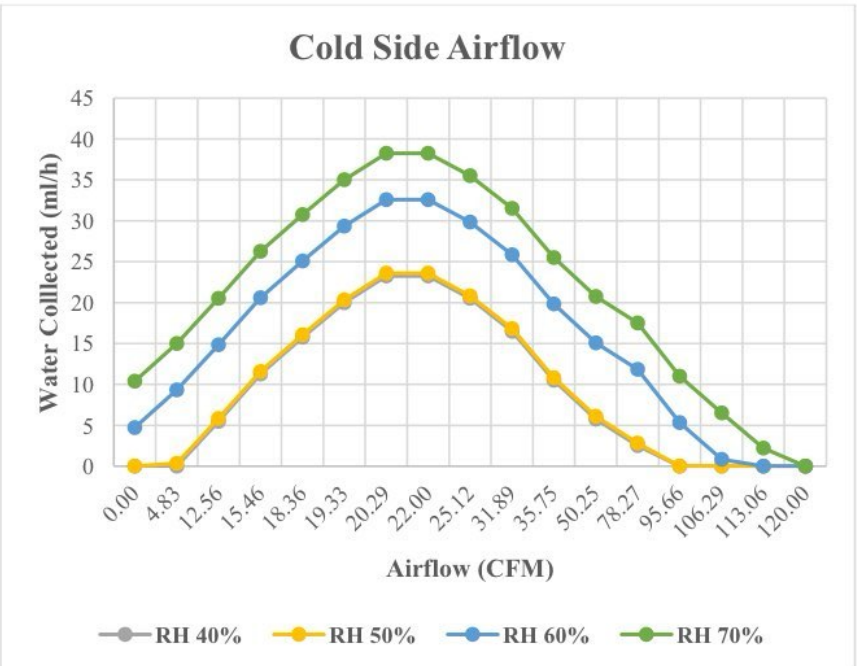

Figure 3.11: The amount of water produced (in ml/h) as a function of forced convection airflow across the fins (in CFM) for various humidity points.

The following experiment was performed at an ambient temperature of 25℃ and optimal fan speed on the hot side and the cold side. The results are shown in Figure 3.12.

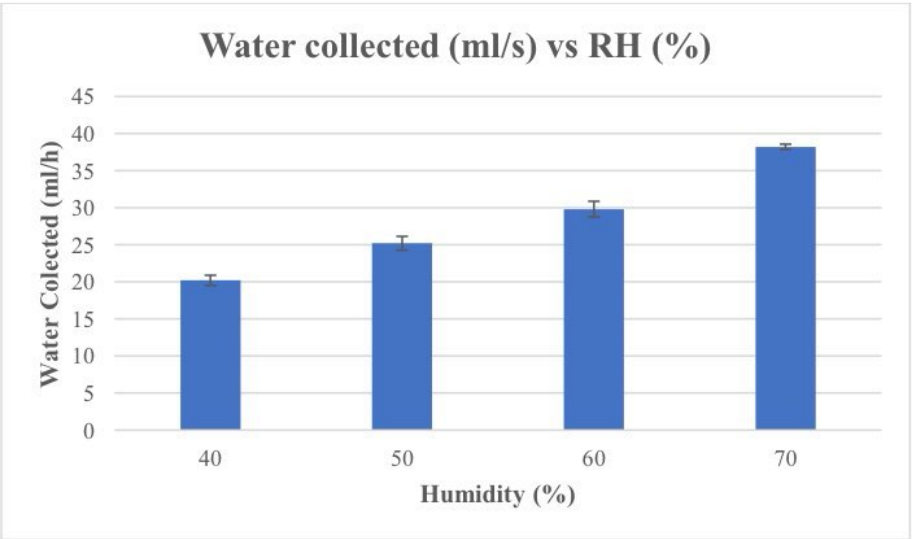

Figure 3.12: Water collected as a function of changing relative humidity at an ambient temperature of (25°C) and optimum forced convection airflow.

Therefore, the optimum airflow input in the cooling channel is 20.29 CFM. Figure 3.13 shows the prototype's output temperature distribution. The prototype was run for optimal conditions for approximately one hour at room temperature of 25°C, 70% relative humidity, input power to the TECs of 54W per TEC, an average 134 CFM airflow on the hot side, and 22CFM input airflow on the cooling chamber.

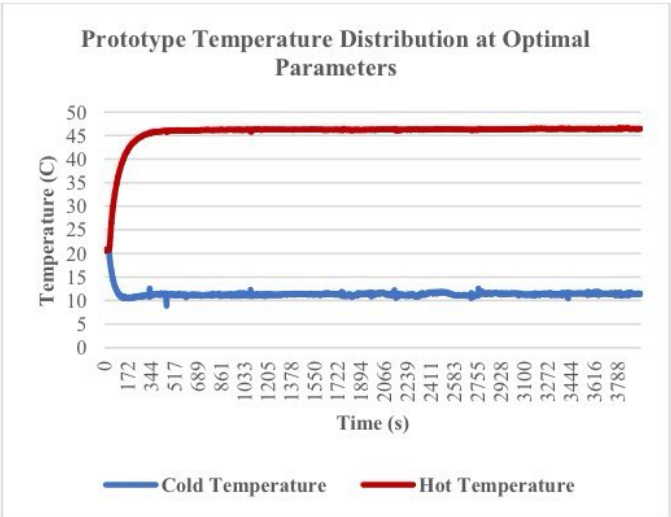

Figure 3.13: Prototype temperature distribution at optimal parameters.

6. Outside Testing

The AWH prototype was tested outside on a clear day between 9:00 am to 5:00 pm. The average ambient temperature was around 18°C (64.4°F), and the ambient humidity was an average of 5%. The fan speed on the hot side and cold sides was set at optimal CFM. Therefore, all three fans on the hot side were set at 135 CFM and on the cold side 2at 2 CFM. The experiment was performed for approximately 2h and 30 mins. A total of 35 ml/h was collected during that time frame, as shown in Figures 3.15 and 3.16. Figures 3.13 and 3.14 show the measured temperatures and humidity during the experiments. The temperature on the hot side of the prototype was 25°C on average and 2°C inside the cooling chamber on average. The moisture inside the cooling chamber was 45% on average. It is important to mention that the temperature on the cold side is lower than the temperature previously shown during the lab testing. This is because the lab ambient temperature was 25 °C, and outside it was 18°C. A significant natural ambiental convection airflow was

present during the outside test. These uncontrolled thermophysical parameters unexpectedly shifted the temperature distribution of the prototype.

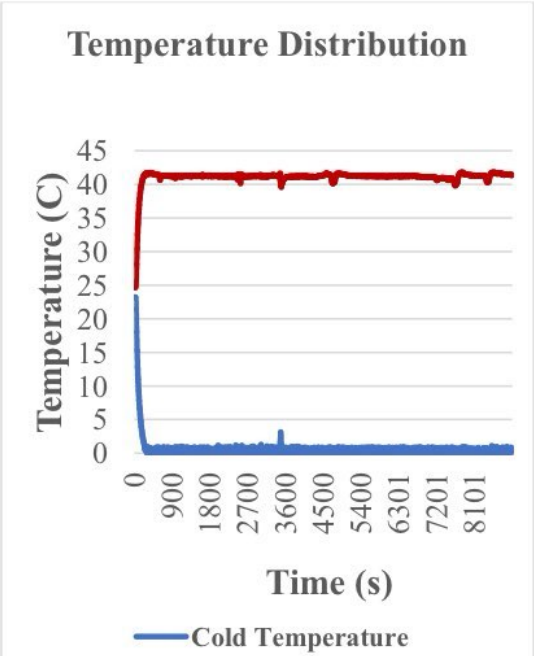

Figure 3.14: Temperature distribution of the prototype tested outside.

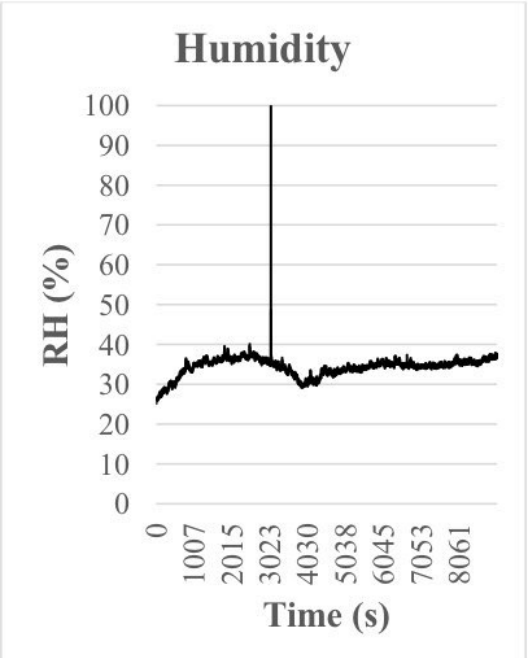

Figure 3.15: Humidity distribution of the prototype tested outside.

Figure 3.16: Cooling Channel of the prototype

Figure 3.17: 30 ml of water collected by the prototype for 2 hours and 30 min.

Table 3.1: Maximum Water collected by similar AWH systems with thermoelectric cooling modules.

Prototype	Water condensed (ml/h)	Relative Humidity (%)	Power consumption (W)	References
Present Study	39 ml/h	70%	67W	This Work
Amir Hossein Shourideh et al.	32 ml/h	60%	60W	"A comprehensive study of an atmospheric water generator using Peltier effect," *Thermal Science and Engineering Progress*, vol. 6, pp. 14–26, Jun. 2018.
Udomskadigool et al.	18.98 ml/h	65-75%	22.8W	"Design optimization of a new hot heat sink with a rectangular fin array for thermoelectric dehumidifiers," Heat Transf. Eng. 28 (2007) 645–655
Vian et al.	45 ml/h	80%	100W	"Numerical modelling and a design of a thermoelectric dehumidifier," Appl. Therm. Eng. 22 (2002) 407–422
Tan and Fok	17 ml/h	79%	124W	"Experimental testing and evaluation of parameters on the extraction of water from air using thermoelectric coolers", J. Test. Eval. 41 (2013) 96–103
Thulfaquir J. et al.	20 ml/h	75%	70W	"Experimental study of atmospheric water collection powered by solar energy using the Peltier effect," *IOP Conf. Ser.: Mater. Sci. Eng.*, vol. 671, no. 1, p. 012155, Jan. 2020.

Table 3.1 shows a comparison of maximum water collection, optimum RH, and power consumption of this designed AWH compared to other similar systems at optimum parameters. The AWH has the second highest water collection rate compared to the other systems, and the third lowest power consumption system.

References

[1] M. A. Muñoz-García, G. P. Moreda, M. P. Raga-Arroyo, and O. Marín-González, "Water harvesting for young trees using Peltier modules powered by photovoltaic solar energy," *Comput. Electron. Agric.*, vol. 93, pp. 60–67, Apr. 2013, doi: 10.1016/j.compag.2013.01.014.

[2] S. Liu *et al.*, "Experimental analysis of a portable atmospheric water generator by thermoelectric cooling method," *Energy Procedia*, vol. 142, pp. 1609–1614, Dec. 2017, doi: 10.1016/j.egypro.2017.12.538.

[3] A. Alenezi and H.-H. Jung, "Design and preliminary experimental testing of a water harvester using the Peltier effect," *J. Korean Soc. Mar. Eng.*, vol. 42, no. 5, pp. 358–363, Jun. 2018, doi: 10.5916/jkosme.2018.42.5.358.

CHAPTER 4: CONCLUSION AND FUTURE OUTLOOK

In summary, the atmospheric water harvester we have introduced is not just a potential solution, but a game-changer for water-scarce regions. By harnessing the cooling capabilities of thermoelectric coolers, this system is designed to efficiently condense water vapor from the air, offering a renewable and reliable source of clean drinking water. Continued thermoelectric materials and cooling technology advancements will further enhance the feasibility and effectiveness of atmospheric water harvesters. Unlike traditional methods such as rainwater collection and dehumidifiers, the Atmospheric water harvester can extract water from the air in any location, regardless of the climate or weather conditions. This unique capability makes it an ideal solution for areas with limited access to clean water, even in the challenging conditions of Nevada.

Looking toward the future, the outlook for atmospheric water harvesters with thermoelectric coolers is increasingly promising. As the global water crisis escalates, the demand for innovative water technologies such as the AWH is expected to increase. However, future improvements to the efficiency of the AWH are still needed. For example, the water collection rate of the system is proportional to the material, the angle of position, and the heat absorption rate of the cold sinks. By further optimizing these three parameters, a significant increase in the efficiency of the AWH will be noticed. This can be done by experimenting with the rate of condensation across different surfaces and at different angled positions to determine the one that yields the most water rate. Some potential candidates are hydrophobic surfaces. This can increase water production by 30% more. The figure of merit of the TECs is also proportional to the coefficient of performance of the AWH. The merit of each TEC is mainly affected by two parameters: the thermal conductivity and the electrical conductivity at the n-p junction. In general, the figure of

merit is high as the thermal conductivity is low and the electrical conductivity is high. However, such a concept is a paradox and challenging to achieve. However, recent developments in nanostructure have led to promising newly developed thermoelectric coolers with high figures of merit. The challenge is in the design and construction. However, a TEC with a high figure of merit significantly impacts the coefficient of performance of the AWH in terms of power reduction and a more significant temperature gradient.

Appendix A: Theoretical MATLAB Modeling of a Single Thermoelectric Module.

```
close all;
clc;

%Loop to change all variables to double
s = whos;
for i = 1:length(s)
    if strcmp(s(i).class,'single')
        name = s(i).name;
        assignin('base', name, double(evalin('base', name)));
    end
end

%Current
I =1;

%Water density as a function of the Temperature (updated with Tave)
pave = 996.3018;

Tamb = 305; %308k 75%
wamb = 0.012366;
ma = 0.0120;
cp = 1025;
density = 1.149;

%Termoelectric Module (Tb-127-2,0-1,05(62))
Imax = 4;
Vmax = 15.4;
```

```
dTmax = 70;
ltec = 44*10^-3;
wtec = 44*10^-3;

%Fixed Parameters
lhole = 9*10^-3;
Hhole = 32*10^-3;
Nhole = 0.008;
tbase = 5*10^-3;
tfin = 3*10^-3;
Nfin = 9;

%denc = 1.281;
%denh = 0.10061;
kfc = 0.0257;%W/mK
kfh = 0.0271;%W/mK
ks = 229;
vc = 15.11*10^-06;%m^2/s
vh = 16.97*10^-06;%m^2/s
Prc = 0.713;
Prh = 0.703;
Ruc = 0.044;
Ruh = 0.044;

lchannel = 431.8*10^-3;
Ntec = 6;
wchannel = 101.6*10^-3;
wfin= 431.8*10^-3;
lfin = 38.1*10^-3;
```

```
Sm = Vmax/Tamb;
Rm = (Vmax*(Tamb-dTmax))/(Tamb*Imax);
Km = (Vmax*Imax*(Tamb-dTmax))/(2*Tamb*dTmax);

%Surface area
At = lhole*lchannel*Nhole+(2*Nhole-2)*Hhole*lchannel;

%Fin area
lc = lfin+tfin/2;

Af = 2*wfin*lc;

%Hydraulic diameter and Reynold Number
Dhyd = (4*lhole*Hhole)/(2*(lhole+Hhole));

Uavec = (ma/Nhole)/(density*lhole*Hhole);

Uaveh = (ma/Nhole)/(density*lhole*Hhole);

Rec = (Uavec*Dhyd)/vc;

Reh = (Uaveh*Dhyd)/vh;

%For cooling
Nuc = 0.023*Rec^0.8*Prc^0.3;

%For heating
Nuh = 0.023*Reh^0.8*Prh^0.4;
```

```
%Convective heat transfer coefficient for cooling/heating
hc = (Nuc*kfc)/Dhyd;
hh = (Nuh*kfh)/Dhyd;

%Fin efficency
Ac = wfin*tfin;
p = 2*(wfin+tfin);

mc = sqrt((hc*p)/(ks*Ac));
nfc = tanh(mc*lc)/(mc*lc);

mh = sqrt((hh*p)/(ks*Ac));
nfh = tanh(mh*lc)/(mh*lc);

%Overal efficiency
noc = 1-(Nfin*Af)/At*(1-nfc);
noh = 1-(Nfin*Af)/At*(1-nfh);

%Resistances
Rt_c = Ruc/(Ntec*ltec*wtec);

Rt_h = Ruh/(Ntec*ltec*wtec);

Rt_base = tbase/(ks*lchannel*wchannel);

Reqc = 1/(noc*At*hc);
Reqh = 1/(noh*At*hh);
```

```
Rc = Reqc+Rt_c+Rt_base;


Rh = Reqh+Rt_h+Rt_base;


%Enthalpy in
hin = cp*(Tamb-273)+wamb*(2501.3+1.86*(Tamb-273))*1000;


fc = (0.790*log(Rec)-1.64)^-2;
dpc = fc*(density*Uavec^2)/(Dhyd)*lchannel;


Pfanc = ma/(density)*dpc;
fh = (0.790*log(Reh)-1.64)^-2;
dph = fh*(density*Uavec^2)/(Dhyd)*lchannel;


Pfanh = ma/(density)*dph;


syms Tc Th Tco Tho Qc Qh Tave P_Tec wc Mw Eff dT COP
eqn1 = ma*(hin-(cp*(Tco-273)+wamb*(2501.3+1.86*(Tco-273))*1000))==(Sm.*I*Tc-
(I.^2*(Rm))/2-Km*(Th-Tc));
eqn2 = ma*cp*(Tho-Tco)==Sm.*I*Th+(1/2).*I.^2*(Rm)-Km*(Th-Tc);
eqn3 = (((Tco-Tc)-(Tamb-Tc))/log((Tco-Tc)/(Tamb-Tc)))/Rc==Sm.*I*Tc-
(1/2).*I.^2*Rm-Km*(Th-Tc);
eqn4 = (((Th-Tco)-(Th-Tho))/log((Th-Tco)/(Th-Tho)))/Rh==Sm.*I*Th+(1/2).*I.^2*Rm-
Km*(Th-Tc);
eqn5 = Qc==((Vmax/Th).*I*Tc-(I.^2*((Vmax*(Th-dTmax))/(Th*Imax)))/2-
((Vmax*Imax*(Th-dTmax))/(2*Th*dTmax))*(Th-Tc))*18;
eqn6 = Qh==((Vmax/Th).*I*Tc+(I.^2*((Vmax*(Th-dTmax))/(Th*Imax)))/2-
((Vmax*Imax*(Th-dTmax))/(2*Th*dTmax))*(Th-Tc))*18;
eqn7 = Tave == (Tco+Tc)/2-273.15;
eqn8 = P_Tec == (Sm.*I*(Th-Tc)+I.^2*Rm)*18;
eqn9 = Qc == ma*(hin-(cp*(Tco-273)+wc*(2501.3+1.86*(Tco-273))*1000));
```

```
eqn10 = Mw == (ma*(wamb-wc)*1000/(pave))*1000000;

eqn11 = Eff == (ma*(wamb-wc)*1000/(pave))*(1/(3.6))/(P_Tec+Pfanh+Pfanc);

eqn12 = dT == Th-Tc;

eqn13 = COP == Qc/P_Tec;


T = vpasolve(eqn1, eqn2, eqn3,
eqn4,eqn5,eqn6,eqn7,eqn8,eqn9,eqn10,eqn11,eqn12,eqn13,[Tc,Th,Tco,Tho,Qc,Qh,Tave,
P_Tec,wc,Mw,Eff,dT,COP]);

%display(T);



Tc1 = double(subs(T.Tc));

Th1 = double(subs(T.Th));

Tco1 = double(subs(T.Tco));

Tho1 = double(subs(T.Tho));

Qc1 = double(subs(T.Qc));

Qh1 = double(subs(T.Qh));

Tave1 = double(subs(T.Tave));

P_TEC1 = double(subs(T.P_Tec));

wc1 = double(subs(T.wc));

Mw1 = double(subs(T.Mw));

Eff1 = double(subs(T.Eff));

dT1 = double(subs(T.dT));

COP1 = double(subs(T.COP));

display(Tave1);

display(Tc1);

T1 = [Tc1 Th1 Tco1 Tho1 Qc1 Qh1 Tave1 P_TEC1 wc1 Mw1 Eff1 dT1 COP1];

%display(T1)

%U = structfun(@subs,T);
```

APPENDIX B: PROTOTYPE ENCACEMENT SCHEMATIC DESIGN